DRAFT VERSION OCTOBER 6, 2020
Preprint typeset using LaTeX style emulateapj v. 12/16/11

ALMaQUEST - IV. THE ALMA-MaNGA QUENCHING AND STAR FORMATION (ALMaQUEST) SURVEY

LIHWAI LIN [1], SARA L. ELLISON [2], HSI-AN PAN [3], MALLORY D. THORP [2], YUNG-CHAU SU [1,4], SEBASTIÁN F. SÁNCHEZ [5], FRANCESCO BELFIORE [6,7], M. S. BOTHWELL [8,9], KEVIN BUNDY [10], YAN-MEI CHEN [11,12], ALICE CONCAS[8,9], BAU-CHING HSIEH [1], PEI-YING HSIEH [1], CHENG LI [13], ROBERTO MAIOLINO [8,9], KAREN MASTERS [14], JEFFREY A. NEWMAN[15,16], KATE ROWLANDS [17,18], YONG SHI [19], REBECCA SMETHURST [20], DAVID V. STARK [14], TING XIAO[21], PO-CHIEH YU [22]

Draft version October 6, 2020

ABSTRACT

The ALMaQUEST (ALMA-MaNGA QUEnching and STar formation) survey is a program with spatially-resolved ^{12}CO(1-0) measurements obtained with the Atacama Large Millimeter Array (ALMA) for 46 galaxies selected from the Mapping Nearby Galaxies at Apache Point Observatory (MaNGA) DR15 optical integral-field spectroscopic survey. The aim of the ALMaQUEST survey is to investigate the dependence of star formation activity on the cold molecular gas content at kpc scales in nearby galaxies. The sample consists of galaxies spanning a wide range in specific star formation rate (sSFR), including starburst (SB), main-sequence (MS), and green valley (GV) galaxies. In this paper, we present the sample selection and characteristics of the ALMA observations, and showcase some of the key results enabled by the combination of spatially-matched stellar populations and gas measurements. Considering the global (aperture-matched) stellar mass, molecular gas mass, and star formation rate of the sample, we find that the sSFR depends on both the star formation efficiency (SFE) and the molecular gas fraction ($f_{\rm H_2}$), although the correlation with the latter is slightly weaker. Furthermore, the dependence of sSFR on the molecular gas content (SFE or $f_{\rm H_2}$) is stronger than that on either the atomic gas fraction or the molecular-to-atomic gas fraction, albeit with the small HI sample size. On kpc scales, the variations in both SFE and $f_{\rm H_2}$ within individual galaxies can be as large as 1-2 dex thereby demonstrating that the availability of spatially-resolved observations is essential to understand the details of both star formation and quenching processes.

Keywords: galaxies:evolution – galaxies: low-redshift – galaxies: star formation – galaxies: ISM

[1] Institute of Astronomy & Astrophysics, Academia Sinica, Taipei 10617, Taiwan; Email: lihwailin@asiaa.sinica.edu.tw
[2] Department of Physics & Astronomy, University of Victoria, Finnerty Road, Victoria, British Columbia, V8P 1A1, Canada
[3] Max-Planck-Institut für Astronomie, Königstuhl 17, D-69117 Heidelberg, Germany
[4] Department of Physics, National Taiwan University, 10617, Taipei, Taiwan
[5] Instituto de Astronomía, Universidad Nacional Autónoma de México, Circuito Exterior, Ciudad Universitaria, Ciudad de México 04510, Mexico
[6] European Southern Observatory, Karl-Schwarzschild-Str. 2, Garching bei München, 85748, Germany
[7] INAF – Osservatorio Astrofisico di Arcetri, Largo E. Fermi 5, I-50157, Firenze, Italy
[8] Cavendish Laboratory, University of Cambridge, 19 J. J. Thomson Avenue, Cambridge CB3 0HE, United Kingdom
[9] University of Cambridge, Kavli Institute for Cosmology, Cambridge, CB3 0HE, UK.
[10] UCO/Lick Observatory, University of California, Santa Cruz, 1156 High St. Santa Cruz, CA 95064, USA
[11] Department of Astronomy, Nanjing University, Nanjing 210093, China
[12] Key Laboratory of Modern Astronomy and Astrophysics (Nanjing University), Ministry of Education, Nanjing 210093, People's Republic of China
[13] Tsinghua Center for Astrophysics and Physics Department, Tsinghua University, Beijing 100084, China
[14] Department of Physics and Astronomy, Haverford College, 370 Lancaster Ave, Haverford, PA 19041, USA
[15] Department of Physics and Astronomy, University of Pittsburgh, 3941 O'Hara Street, Pittsburgh, PA 15260, USA
[16] Pittsburgh Particle physics, Astrophysics, and Cosmology Center (PITT PACC)
[17] Space Telescope Science Institute, 3700 San Martin Dr Baltimore, MD 21218, USA
[18] Department of Physics & Astronomy, Johns Hopkins University, Bloomberg centre, 3400 N. Charles St., Baltimore, MD 21218, USA
[19] School of Astronomy and Space Science, Nanjing University, Nanjing 210093, China
[20] Oxford Astrophysics, Department of Physics, University of Oxford, Denys Wilkinson Building, Keble Road, Oxford, OX1 3RH, UK
[21] Department of Physics, Zhejiang University, Hangzhou, Zhejiang 310027, China
[22] Yuan Ze University College of General Studies

1. INTRODUCTION

Star-forming galaxies are known to form a tight relationship in the total star formation rate (SFR) – total stellar mass (M_*) plane, dubbed the global star forming main sequence (SFMS or MS; Brinchmann et al. 2004; Noeske et al. 2007; Elbaz et al. 2007; Daddi et al. 2007; Whitaker et al. 2012). The normalization, shape, and scatter of the SFMS are found to depend on environment, morphology, and the redshift of galaxies (e.g., Lin et al. 2012; Whitaker et al. 2012; Koyama et al. 2013; Lin et al. 2014; Speagle et al. 2014; Jian et al. 2018). As star formation is regulated by both the amount of available gas and internal feedback processes, mapping the molecular gas, which is the fuel for star formation, is therefore key to understanding how galaxies evolve within and across the global SFMS. Likewise, the molecular gas content holds important clues as to why galaxies eventually halt their star formation and become quiescent.

The COLD GASS survey (CO Legacy Database for GASS, Saintonge et al. 2011) was the first systematic CO survey for hundreds of local galaxies with $M_* > 10^{10} M_\odot$. The 'extended' COLD GASS (xCOLD GASS, Saintonge et al. 2017) pushed the sample down to $M_* > 10^9 M_\odot$, providing ^{12}CO(1-0) measurements for 532 galaxies in combination with the original COLD GASS sample. With this large set of galaxies, Saintonge et al. (2017) found that the offset from the star forming main sequence is correlated strongly with both the molecular gas to stellar mass ratio (defined as $f_{H_2} = M_{H_2}/M_*$, which we simply refer to as molecular gas fraction for the rest of this paper) and the star formation efficiency (SFE = SFR/M_{H_2}). In other words, the elevation or suppression of star formation rate not only depends on the availability of gas but also on the conditions in the interstellar medium (see also Huang & Kauffmann 2014; Tacconi et al. 2013, 2018; Piotrowska et al. 2020). The ALLSMOG (APEX low-redshift legacy survey for molecular gas) survey (Bothwell et al. 2014; Cicone et al. 2017) complements the COLD GASS sample in the low mass regime by observing a further 88 nearby star-forming galaxies with the stellar masses between $10^{8.5}$ and $10^{10} M_\odot$ using the APEX telescope. The combination of xCOLD GASS and ALLSMOG samples reveals that the CO luminosity not only strongly correlates with stellar mass and SFR but also varies with other factors, such as metallicity and HI mass (hereafter M_{HI}; Cicone et al. 2017).

While surveys such as xCOLD GASS and ALLSMOG enable the exploration of the connection between the global gas content and SFR across a wide range of galaxy properties, as well as the variation of gas properties with respect to their positions on the SFR– M_* plane, details of the physical processes that shape the SFMS and its evolution remain unclear. To take a step further, spatially resolved observations are required for three main reasons: 1) There is growing evidence that the SFR also traces M_* at kpc scales (Sánchez et al. 2013; Wuyts et al. 2013; Cano-Díaz et al. 2016; Hsieh et al. 2017; Abdurro'uf & Akiyama 2017; Pan et al. 2018; Ellison et al. 2018; Medling et al. 2018; Vulcani et al. 2019; Cano-Díaz et al. 2019; Wang et al. 2019; Morselli et al. 2020). This relation has been dubbed the 'resolved' SFMS (rSFMS) and its existence suggests that the well-known global star forming main sequence may be an ensemble effect of local processes; 2) Star formation takes places within giant molecular clouds (GMCs), whose sizes are on the order of hundreds of pcs or even smaller. The star formation law that characterizes the relation between SFR and gas density, often referred to as the Schmidt-Kennicutt relation (or SK relation, Schmidt 1959; Kennicutt 1998), is also found to vary with the substructures of galaxies and galactocentric radius (e.g., Bigiel et al. 2008; Leroy et al. 2013; Usero et al. 2015; Rahmani et al. 2016; Utomo et al. 2017; Schinnerer et al. 2019; Chevance et al. 2020); 3) The spatial sequence of quenching (inside-out vs. outside-in vs. global) obtained from Integral Field Spectroscopy (IFS) observations provides powerful constraints on quenching mechanisms (González Delgado et al. 2014, 2016; Tacchella et al. 2015; Li et al. 2015; Ellison et al. 2018; Sánchez et al. 2018; Lin et al. 2019a, also see Sánchez 2020 for a review), particularly when combined with resolved gas observations (Lin et al. 2017). Obtaining a full picture of how the star formation is related to the global properties of galaxies and how it is quenched therefore requires mapping stars and gas in galaxies with sufficient spatial resolution and sensitivity.

Recent spatially-resolved observational programs, such as the EDGE (the Extragalactic Database for Galaxy Evolution)-CALIFA (Calar Alto Legacy Integral Field Area) survey and the PHANGS (Physics at High Angular resolution in Nearby GalaxieS)-MUSE survey, are designed to combine the power of optical IFS and millimeter-wave interferometry observations to address key questions in star formation. The EDGE-CALIFA survey (Bolatto et al. 2017) observed 126 CALIFA-selected galaxies in ^{12}CO(1-0) and ^{13}CO(1-0) using the Combined Array for Millimeter-wave Astronomy (CARMA) with an spatial resolution ($\sim$ 1.4 kpc) matched to CALIFA. This dataset enables studies of the relationships between molecular gas, stellar mass, star formation rate, metallicity, and dust extinction on kpc scales and their dependence on the global galaxy properties in a fairly large and representative local sample (e.g., Utomo et al. 2017; Colombo et al. 2018; Dey et al. 2019; Barrera-Ballesteros et al. 2020). The PHANGS-MUSE project observed 19 nearby galaxies selected from a subset of the PHANGS-ALMA survey (A. K. Leroy et al. 2020, in preparation), utilizing the Multi Unit Spectroscopic Explorer (MUSE) at the VLT. Both ALMA and MUSE observations achieve an angular resolution $\sim 1''$, which corresponds to a physical scale of < 100 pc in their sample. Although modest in sample size, PHANGS-MUSE therefore offers exquisite spatial resolution. Combined, EDGE-CALIFA and PHANGS-MUSE offer complementary strengths for studying gas and star formation in the nearby universe.

While both EDGE-CALIFA and PHANGS-MUSE offer exceptional opportunities to study physical processes that govern star formation at (sub)kpc scales, these samples mostly lie on the star-forming main sequence and hence do not cover a sufficiently wide range in specific star formation rates (sSFR) to study the full gamut of processes from starbursts to quenching. In order to systematically understand the processes driving and regulating star formation, it is desirable to also include galaxies that are beyond the main sequence (in both directions). To test the feasibility of detecting resolved (kpc-scale) CO in green valley galaxies, in Lin et al. (2017) we conducted a pilot ALMA study of three MaNGA-selected galaxies. It was found that the molecular gas fraction [23] and SFE respond differently between bulge and disk regions as

[23] In Lin et al. (2017), the molecular gas fraction is defined as $M_{H_2}/(M_*+M_{H_2})$, slightly different from M_{H_2}/M_* used in this paper. The difference, however, is small as M_{H_2} is in general less than 10% of M_* in our sample.

galaxies move away from the main sequence: the molecular gas fraction shows a stronger decline with respect to sSFR in bulges than in disks whereas SFE is reduced in both the bulge and disk regions (Lin et al. 2017), consistent with inside-out quenching.

In this paper, we introduce the ALMA-MaNGA QUEnching and STar formation survey (ALMaQUEST), which expands the pilot sample of Lin et al. (2017) by more than an order of magnitude, covering not only main -sequence galaxies, but also starburst and green valley galaxies, all selected from the MaNGA survey. ALMaQUEST was designed to provide an extensive picture of the relationship between stellar populations, SFR, and gas at kpc scales by taking advantage of IFS data from MaNGA and resolved ^{12}CO(1-0) observations from ALMA. Some of the main scientific questions that we aim to address with the ALMaQUEST survey include: 1) How are the properties of a galaxy's gas content linked to the resolved SFMS? 2) What are the primary physical mechanisms responsible for quenching? 3) Are starbursting galaxies driven by elevated $f_{\rm H_2}$ or enhanced SFE?

This work is a presentation of the ALMaQUEST data that can be used as a companion to the various science papers. In §2, we describe the survey design, sample selections, and the data products used in this work. §3 characterizes both the global and local molecular gas properties of the sample. Some example science cases enabled by this sample are described in §4. A summary of this work is given in §5.

Throughout this paper we adopt the following cosmology: H_0 = 70 km s^{-1} Mpc^{-1}, $\Omega_{\rm m}$ = 0.3 and Ω_Λ = 0.7. We use a Salpeter initial mass function (IMF).

2. SAMPLE AND OBSERVATIONS

2.1. *Sample Selection*

The ALMaQUEST survey consists of ALMA ^{12}CO(1-0) observations of galaxies selected from the MaNGA survey (Bundy et al. 2015; Yan et al. 2016b). ALMaQUEST compiles datasets from four individual ALMA programs– 2015.1.01225.S, 2017.1.01093.S, 2018.1.00558.S (PI: Lin), and 2018.1.00541.S (PI: Ellison). It contains 46 unique galaxies with a wide range of sSFR, spanning from the the green valley (hereafter GV), main sequence (hereafter MS), and up to the starburst (hereafter SB) regimes. While the majority of the targets are selected according to their global sSFR, the 12 SB galaxies are required to lie on or above the main sequence and show elevated SFR relative to the control sample within 0.5 R_e by at least 50 percent (see Ellison et al. 2020a, for details). All of these observations adopt identical observing setups and reduction procedures. The locations of the 46 galaxies and all the MaNGA Data Release 15 (DR15) galaxies in the global SFR and M_* plane are shown in Figure 1. The global measurements of SFR and M_* are taken from the PIPE3D (Sánchez et al. 2016a,b) value-added catalog (Sánchez et al. 2018), which sums the MaNGA spaxel measurements across the data cubes. Some basic quantities of the 46 ALMaQUEST galaxies are given in Table 1. Key information and characteristics of the ALMaQUEST survey can be found in the ALMaQUEST webpage: http://arc.phys.uvic.ca/∼almaquest/.

2.2. *MaNGA Data*

MaNGA is an IFS survey conducted with the SDSS 2.5m telescope (Gunn et al. 2006), as part of the SDSS-IV survey (Albareti et al. 2017; Blanton et al. 2017). The MaNGA parent sample is selected to form an approximately-uniform distribution in *i*-band absolute magnitude, which corresponds to a roughly flat distribution in *log* M_* (Wake et al. 2017). MaNGA uses the BOSS spectrographs (Smee et al. 2013) and couples them with hexagonal fibre bundles of different sizes (Drory et al. 2015). Each spectrum covers a wavelength range of 3500-10,000Å with a spectral resolution ∼60 kms^{-1}. After dithering, MaNGA data have an effective angular resolution (full width at half maximum; FWHM) of 2.5″(Law et al. 2015), corresponding to a physical scale of 0.5-6.5 kpc. Data cubes are grided with 0.5″spaxels. The methods used for sky subtraction and spectrophotometric calibration are described in Law et al. (2016) and Yan et al. (2016a), respectively.

The MaNGA data used in this work is based on the SDSS Data Release 15 (DR15) version processed by the MaNGA reduction pipeline (Law et al. 2016). Measurements of the Σ_* and emission-line fluxes are taken from the public PIPE3D data products (Sánchez et al. 2016a, 2018). The stellar mass is obtained based on the best-fit stellar population model that describes the stellar continuum of a given spectrum. The best-fit stellar continuum is then subtracted from the reduced spectrum in order to obtain the emission line measurements. All the emission lines were extinction corrected using the Balmer decrement computed at each spaxel and a Milky Way extinction curve with Rv = 3.1 (Cardelli et al. 1989). The SFR is estimated based on this extinction corrected Hα flux following the conversion given by Kennicutt (1998) with a Salpeter IMF. Σ_* and $\Sigma_{\rm SFR}$ are computed using the stellar mass and SFR derived for each spaxel, normalized to the physical area of one spaxel with an inclination correction derived using the axis ratio from the NASA Sloan Atlas (NSA) catalog [24]. We classify each MaNGA spaxel into regions where the dominant ionizing source is star formation, LI(N)ER , or Seyfert using the BPT diagnostic based on the [OIII]/Hβ vs. [SII]/Hα line ratios (Kewley et al. 2001, 2006). We require a signal to noise (S/N) > 3 for the Hα and Hβ lines and S/N > 2 for the [OIII] and [SII] lines when performing this classification.

2.3. *ALMA Observations*

Molecular gas observations in ^{12}CO(1-0) (rest frame 115.271204 GHz) were carried out with ALMA during Cycle 3, 5, and 6 using the Band 3 receiver. The observations were taken in the C43-2 configuration (synthesized beam FWHM ∼ 2.5″), thus matching the MaNGA resolution. We used a single pointing with a field-of-view (FOV) of ∼ 50″. The largest structure that we expect to be sensitive to is about 23″ (∼14 kpc). Our spectral setup includes one high-resolution spectral window (∼ 10 km s^{-1}) targeting ^{12}CO(1-0), and one to three low-resolution spectral window(s) (∼ 90 km s^{-1}) around the target line aimed at detecting/studying the continuum. On-target integration time varies from 0.2 to 2.5 hours and is set to have a S/N (CO) greater than 3 for more than 50% of spaxels with S/N (Hα) > 3. This setup was empirically shown in our pilot program (Lin et al. 2017) to be a good compromise between the required integration time and the number of spaxels sufficient for carrying out statistically meaningful analyses. The actual sensitivity achieved for individual sources is given in Table 1. The data were calibrated using the ALMA data reduction software CASA version 4.5 or 5.4 (Common Astronomy Software Applications;

[24] http://nsatlas.org/

McMullin et al. 2007) and standard ALMA pipeline[25]. The systematic flux uncertainty associated with the calibration is typically 5 – 10% in Band 3. Continuum is subtracted from the data in the visibility domain. Out of 46 ALMaQUEST objects, 4 (PLATEIFUs: 8084-3702, 8155-6101, 8615-3703, 8655-3701) are detected in the continuum.

The task CLEAN was employed to clean the continuum-subtracted data down to 1σ and produce spectral line data cubes using Briggs weighting with a robust parameter of 0.5. The resultant native effective beamsize for each target ranges from $1.6''$ to $2.8''$. 28 out of 46 galaxies have a native effective beamsize comparable to the point spread function (PSF) of MaNGA ($2.5'' \pm 10\%$), 14 galaxies have beamsize $\leqslant 2.3''$, and 4 have beamsizes $\sim 2.8''$. In order to facilitate the comparison between ALMA and MaNGA, we re-imaged the data and adopted a user-specified pixel size ($0.5''$) and restoring beamsize ($2.5'' \times 2.5''$) to match the image grid and the spatial resolution of the MaNGA images. The final cubes have channel widths of 11 km s^{-1} and rms noise ($\sigma_{\rm rms}$) of ~ 0.2 – 2 mJy beam^{-1}. The difference in $\sigma_{\rm rms}$ between the data cube with the original beamsize and our user-specified beamsize is as small as $< 5\%$ because the original beamsize and the user-specified beamsize are not significantly different.

In Figure 2, we show the 46 continuum-subtracted ALMA spectra centered on the position of the CO (1-0) line using the systematic velocity derived from the optical MaNGA redshift, integrated over the region enclosed by 1.5 effective radius (R_e). The 0th – 2nd moment maps (0th: integrated intensity, 1st: intensity-weighted velocity field, and 2nd: intensity-weighted velocity dispersion) were constructed by using the task IMMOMENTS in CASA. The integrated intensity maps were created by integrating emission from a velocity range set by hand to match the observed line profile shown in Figure 2 without any clipping in signal. Data in this velocity range were also used to generate velocity field and dispersion maps, with a 4σ clipping applied to avoid noise contamination.

2.4. *GBT HI Observations*

HI-MaNGA is an HI follow-up campaign for the MaNGA survey. Complete details can be found in (Masters et al. 2019) which we briefly summarize here.

HI-MaNGA uses the Green Bank Telescope to observe MaNGA galaxies at $z < 0.05$ lacking overlap with the ALFALFA survey (Haynes et al. 2018). The upper redshift limit is applied due to the declining sensitivity beyond this redshift. Observations are conducted in position-switching mode using the L-band receiver and VEGAS backend for a total (ON+OFF) time of 30 minutes per target. These integration times yield typical rms noise levels of 1.5-2 mJy after boxcar and hanning smoothing to a spectral resolution of $\sim$10 km s^{-1} .

HI-MaNGA data are reduced (including RFI flagging, smoothing, and baseline removal) using GBTIDL. The spectra are visually inspected for the presence of an HI emission line, and in the case of a detection the flux, linewidth, and central velocity of the spectral line are measured. For non-detections, a 3σ upper limit is estimated assuming a linewidth of 200 km s^{-1} . Fluxes and upper limits are converted to HI masses using $M_{\rm HI}$ = 2.36e5$\times$(D / Mpc)$^2 \times S_{21}$, where S_{21} is the flux of 21cm emission line in units of Jy km s^{-1} .

[25] 7977-12705, 7977-3704, and 7977-9101 were calibrated with CASA version 4.5 because they were observed in an earlier cycle.

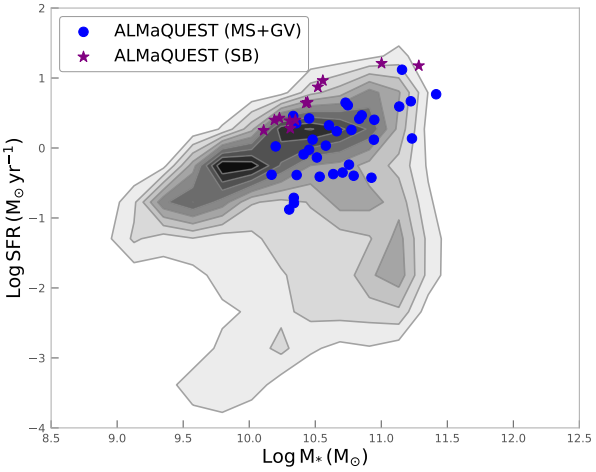

Figure 1. Distribution of the 46 ALMaQUEST galaxies (symbols) and all MaNGA DR15 galaxies (grey contours) in the global SFR and M_* plane. SFR and M_* are taken from the PIPE3D DR15 output. The purple stars and blue circles represent the starburst (Ellison et al. 2020a) and the remaining ALMaQUEST targets, respectively.

Among the 46 ALMaQUEST galaxies, 26 and 7 galaxies are included in the HI-MaNGA and ALFALFA samples, respectively. In this study, we use the HI data from both the second data release of HI-MaNGA (D. Stark et al. in prep.) and the ALFALFA catalog (Haynes et al. 2018).

2.5. *Global Measurements*

In Tables 2 – 3, we provide several key measurements for the 46 ALMaQUEST galaxies, including the area enclosed within 1.5 R_e, stellar mass, star formation rate, CO flux, H_2 mass, sSFR, SFE, and f_{H_2}. These integrated quantities are estimated in two ways: 1) By summing up the measured values over the area enclosed by 1.5 R_e and 2) by summing over the areas within the MaNGA bundles. These values are given in Table 2 and Table 3, respectively. The choice of 1.5 R_e is driven by the bundle coverage of MaNGA observations as two-third of the MaNGA sample is required to be covered by the MaNGA IFU out to 1.5 R_e and one-third of the sample is covered out to 2.5 R_e (Wake et al. 2017).

The H_2 mass is computed from the CO flux by adopting a constant conversion factor ($\alpha_{\rm CO}$) of 4.35 M$_\odot$(K km s^{-1} pc^2)$^{-1}$ (e.g., Bolatto et al. 2013). We will discuss the effect of adopting a metallicity-dependent conversion factor in later sections (§3.1 and §3.3). For the SFR measurement, only spaxels classified as star-forming using the [SII] BPT diagnostic (Kewley et al. 2001, 2006) are included in this study.

3. RESULTS

Having introduced the characteristics of the ALMaQUEST survey and the associated data products, in this section we present the molecular gas contents of ALMaQUEST galaxies and their relationships with the stellar populations, both globally and locally.

3.1. *The integrated (global) scaling relations–SFR,* M_**, and* M_{H_2}

It has been pointed out that the position of galaxies in the global SFR– M_* plane is driven by the combination of variations in both f_{H_2} and SFE (e.g., Tacconi et al. 2013; Sargent

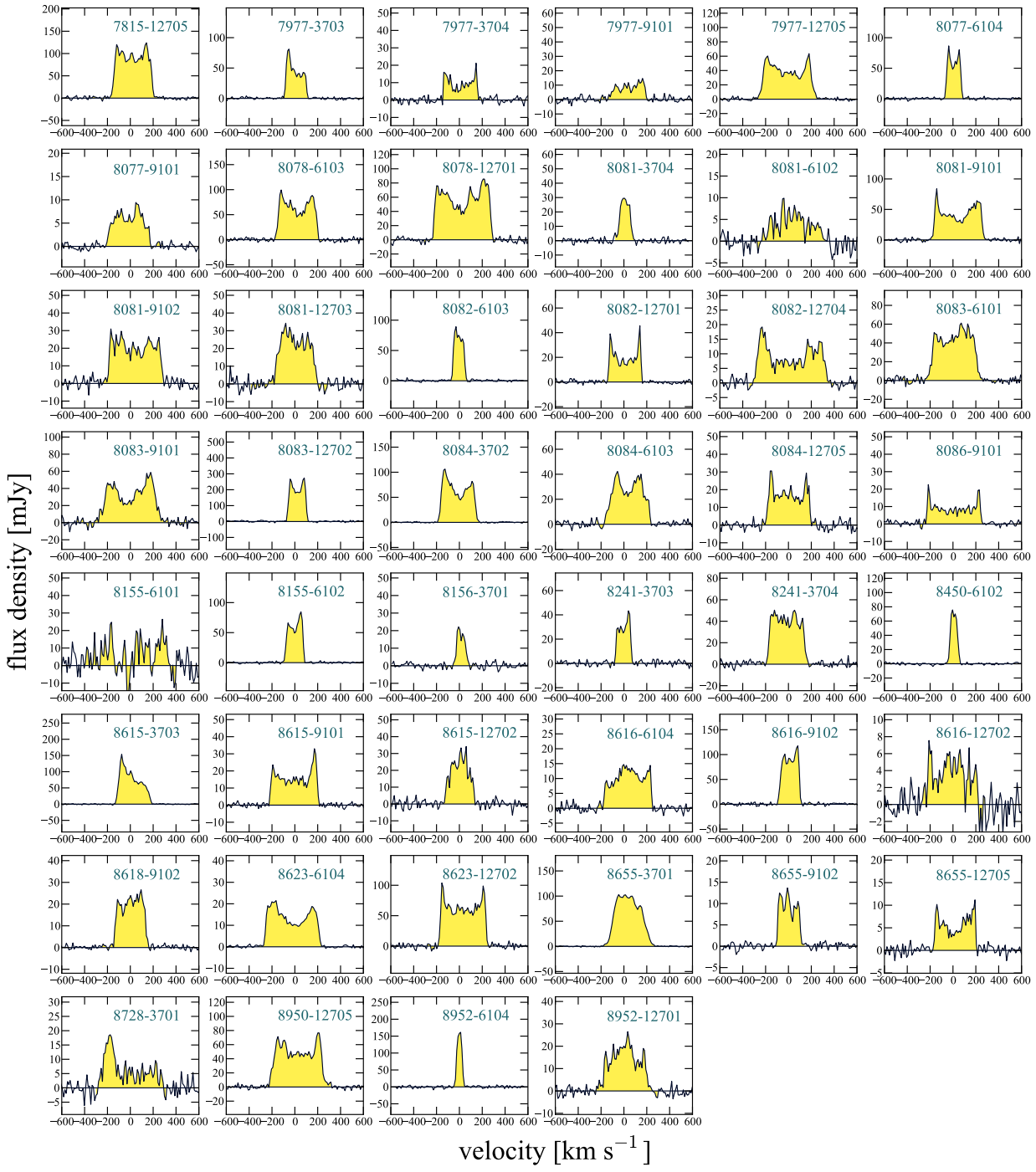

Figure 2. ^{12}CO(1-0) spectra integrated over the area enclosed by the 1.5 R_e for 46 ALMaQUEST galaxies. The yellow shaded areas represent the region of the spectrum used for computing the line flux. The MaNGA plate-IFU identifier is given in the upper right of each panel.

et al. 2014; Saintonge et al. 2016, 2017). In this subsection, we present the relations between the integrated quantities, i.e., the total SFR, total stellar mass, and the total H_2 mass, for the ALMaQUEST sample. Particularly, we investigate whether the variation in sSFR is primarily driven by the change in SFE or f_{H_2}. In Figure 3, we present the correlations among the global SFR, M_*, and M_{H_2}, measured within the areas enclosed by $1.5R_e$ as given in Table 2 (hereafter referred to as the aperture-matched measurements), although we note that the trends shown in Figure 3 remain unchanged if the MaNGA bundle-integrated properties (Table 3) are used. In all the three panels, the typical uncertainties in each measurement are shown in the upper-left corners. For SFR and M_*, the uncertainties represent the typical errors in the SFR and M_* measurements, whereas the uncertainty in M_{H_2} takes into account both the measurement error and the uncertainty in the CO-to-M_{H_2} conversion factor with the latter being the dominant factor (see the end of this section).

The top panel of Figure 3 shows the aperture-matched SFR versus M_* (within $1.5R_e$) for the ALMaQUEST sample (blue symbols). We also overplot the distributions of the xCOLD GASS sample (Saintonge et al. 2017) shown as the grey sym-

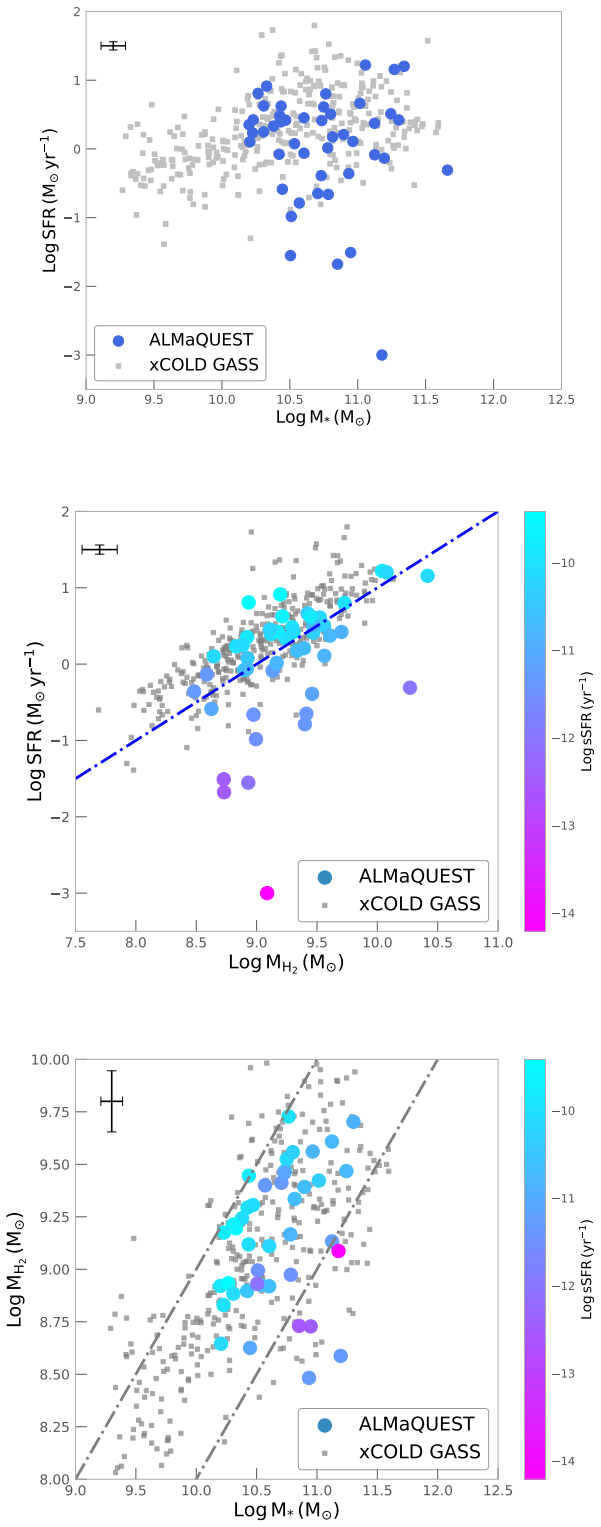

Figure 3. Top panel: Distribution of the ALMaQUEST galaxies (blue symbols) in the global SFR and M_* plane. For comparison, the xCOLD GASS sample is shown as the grey squares and only galaxies with CO detections are shown for clarity. Middle panel: distribution of the ALMaQUEST galaxies in the global Schmidt-Kenicutt relation (SFR vs. M_*) color-coded by sSFR. The blue dot-dashed line corresponds to the SFE = 10^{-9} yr^{-1} line, not the best-fit to the data. Bottom panel: Relation between the global M_{H_2} and M_* (global molecular gas main sequence) of the ALMaQUEST sample color-coded by sSFR. The two grey dot-dashed lines, from left to right, show a gas-to-stellar ratio of 0.1 and 0.01, respectively. For the three panels, all of the ALMaQUEST quantities (i.e., SFR, M_* , M_{H_2}) are computed within 1.5 R_e. The black error bars shown in the upper left corners represent the typical uncertainties.

bols [26]. An offset of 0.26 dex has been added to the xCOLD GASS SFR and M_* measurements to account for the conversion from the Chabrier to the Salpeter IMF. For xCOLD GASS, only galaxies detected in CO are shown here for clarity. The top panel of Figure 3 is analogous to the SFR versus M_* plot shown in Figure 1 but differs in the sense that the measurements in the latter are output by PIPE3D, which integrates values over the entire MaNGA bundle data cubes and uses all spaxels regardless their BPT classifications, whereas here we only consider star-forming spaxels within 1.5R_e. As a result, the SFR distribution is generally lower in Figure 3 compared to that in Figure 1. Some galaxies with very few star-forming spaxels even have substantially lower sSFR compared to the PIPE3D output. It can be seen that while most of the ALMaQUEST galaxies remain in the MS and GV regimes, there are, however, a few (∼5) galaxies falling into the quiescent population.

The middle panel of Figure 3 displays the global Schmidt-Kennicutt relation for the ALMaQUEST sample, color-coded by the sSFR. The blue line represents a gas depletion time (1/SFE) of 1 Gyr to guide the eye. It can be seen that galaxies with higher (lower) sSFR tend to populate on the upper (lower) end of the SFR – M_{H_2} relation, suggesting a strong role of SFE in determining the sSFR of galaxies. This is in good qualitative agreement with previous studies on the global molecular gas content, which have found a strong relationship between SFE and sSFR (e.g., Huang & Kauffmann 2014; Saintonge et al. 2017; Bolatto et al. 2017).

In the bottom panel of Figure 3, we show M_{H_2} as a function of M_*, which is the global version of the molecular gas main sequence (MGMS, Lin et al. 2019b). It was previously found that these two quantities for typical star-forming galaxies are almost linearly correlated with each other (e.g. Cicone et al. 2017). As our sample consists of both galaxies on and below the SFMS, we are able to explore how galaxies with different sSFR populate in this diagram. It can be seen that at a fixed sSFR, there appears to be a large spread in the molecular gas-to-stellar mass ratio, i.e. f_{H_2}, and vice versa. The variation in sSFR with respect to f_{H_2} is hence less obvious compared to that with respect to SFE. We also notice that while the galaxies with sSFR < 10^{-11} yr^{-1} span a wide range in terms of the molecular gas-to-stellar mass ratio, their values extend to the regime below 1%, suggesting a strong depletion of molecular gas within 1.5R_e in some of the galaxies with low sSFR.

To better quantify the relative contributions between SFE and f_{H_2} to the sSFR, Figure 4 shows the correlations between sSFR with respect to SFE (left panel) and f_{H_2} (right panel). The ALMaQUEST and xCOLD GASS measurements are shown in blue and grey symbols, respectively. It can be seen that both samples follow very similar trends, although the ALMaQUEST survey shows several outliers from the sSFR vs. f_{H_2} relation. This is likely due to the fact that the CO-detected sample of the ALMaQUEST extends to lower sSFR regime. The Kendall correlation analysis for the ALMaQUEST sample shows that the correlation between sSFR and SFE (τ = 0.67) is slightly stronger compared to that between sSFR and f_{H_2} (τ = 0.54). However, one potential caveat in interpreting this result is that the SFE spans a much wider range (4 orders of magnitude) than the f_{H_2} does, owing to the inclusion of a datapoint with SFE ∼ -12. To test if the tighter correlation seen in the sSFR vs. SFE is driven by the dy-

[26] We note that the xCOLD GASS measurements are not made strictly within 1.5Re and thus the data are not entirely comparable.

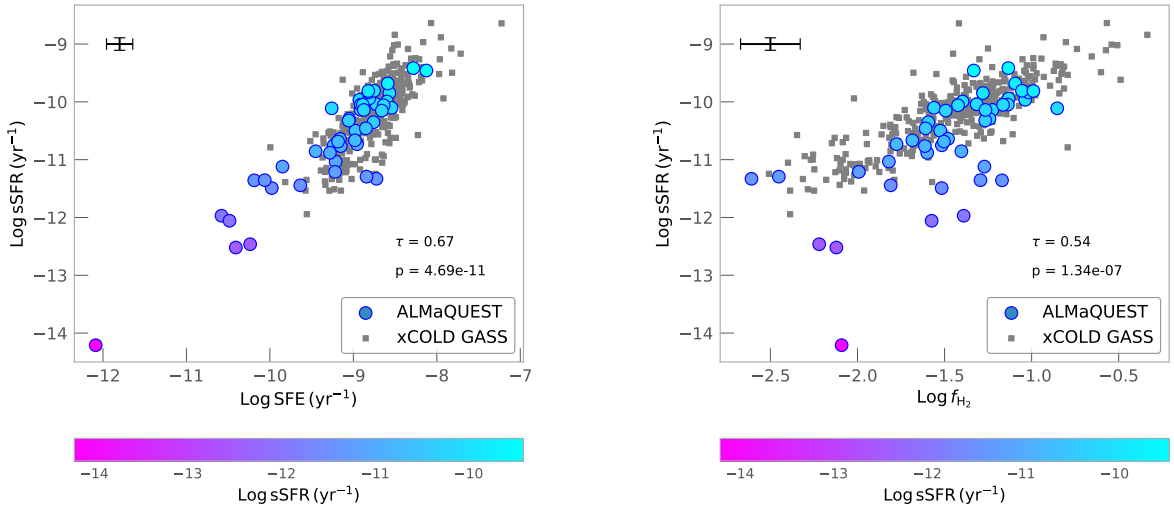

Figure 4. The global sSFR of ALMaQUEST galaxies (blue circles) and xCOLD GASS (grey squares) as a function of SFE (left panel) and f_{H_2} (right panel). For both panels, all of the ALMaQUEST quantities (i.e., SFR, M_* , M_{H_2}) are computed within 1.5 R_e. The black error bars shown in the upper left corners represent the typical uncertainties. The Kendall correlation coefficient (τ) and p-value are shown in the legend.

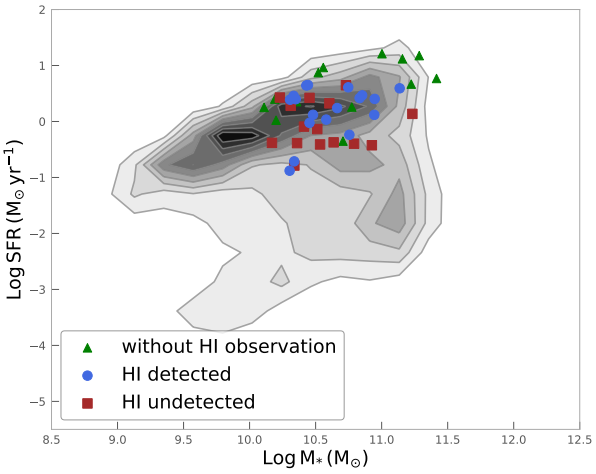

Figure 5. Distribution of the 46 ALMaQUEST galaxies (symbols) in the global SFR vs. M_* (taken from the PIPE3D DR15 output) plane, color-coded by their status of HI observations (blue: with HI detection; brown: without HI detection; green: no observation). The full MaNGA DR15 galaxies are shown in grey contours.

namical range effect, we repeat the analysis by excluding the lowest SFE datapoint. We find that the τ value only slightly decreases from 0.67 to 0.66 in this case and remains greater than the correlation between sSFR and f_{H_2}. In summary, both SFE and f_{H_2} contribute to the variation in sSFR of galaxies, although SFE is found to play a slightly stronger role in governing the sSFR of galaxies. A similar trend has also been seen in previous studies, which found a comparable contribution of f_{H_2} and SFE in the regulation (e.g. Saintonge et al. 2017; Piotrowska et al. 2020).

As described in §2.5, the global SFR here are estimated using the star-forming spaxels classified with the [SII] BPT diagnostic (Kewley et al. 2001, 2006). To test if our results are stable against different choices of area types included in the SFR calculation, in the Appendix we also show the results using all spaxels or an alternative BPT classification scheme based on the [NII] diagnostic (Kauffmann et al. 2003). The former has a caveat that the total SFR can be overestimated since the non-star forming spaxels where the Hα emissions powered by non-star formation mechanisms are also included. In both cases, we also see positive correlations between sSFR and SFE and between sSFR and f_{H_2}. While the dependence of sSFR on SFE or f_{H_2} are comparable in the case of all spaxels considered, the correlation with respect to SFE is found to be slightly stronger than with respect to f_{H_2} in the case where only [NII] BPT classified star-forming spaxels are included, in good agreement with the result based on the [SII] BPT method.

We note that our results described above are drawn based on a constant value of α_{CO}. To examine the potential effect of this assumption, we also consider two types of varying α_{CO}, one taken from Sun et al. (2020), which takes into account the metallicity dependence alone, and the other from Narayanan et al. (2012), which considers the dependence on both the CO line intensity and metallicity. In the first method, we adopt Eq. (4) of Sun et al. (2020):

$$\alpha_{CO} = 4.35(Z/Z_\odot)^{-1.6}\ M_\odot\ pc^{-2}(K\ km\ s^{-1})^{-1}, \quad (1)$$

where Z is the (linear) gas phase abundance and $Z_\odot$ is the solar value. The gas phase metallicity in log can be calculated through the O3N2 calibrator (Pettini & Pagel 2004):

$$12+\log(O/H) = 8.73-0.32\times O3N2. \quad (2)$$

In the second method, we utilize Eq. (11) of Narayanan et al. (2012):

$$\alpha_{CO} = \frac{\min[6.3, 10.7\times W_{CO}^{-0.32}]}{(Z/Z_\odot)^{0.65}}, \quad (3)$$

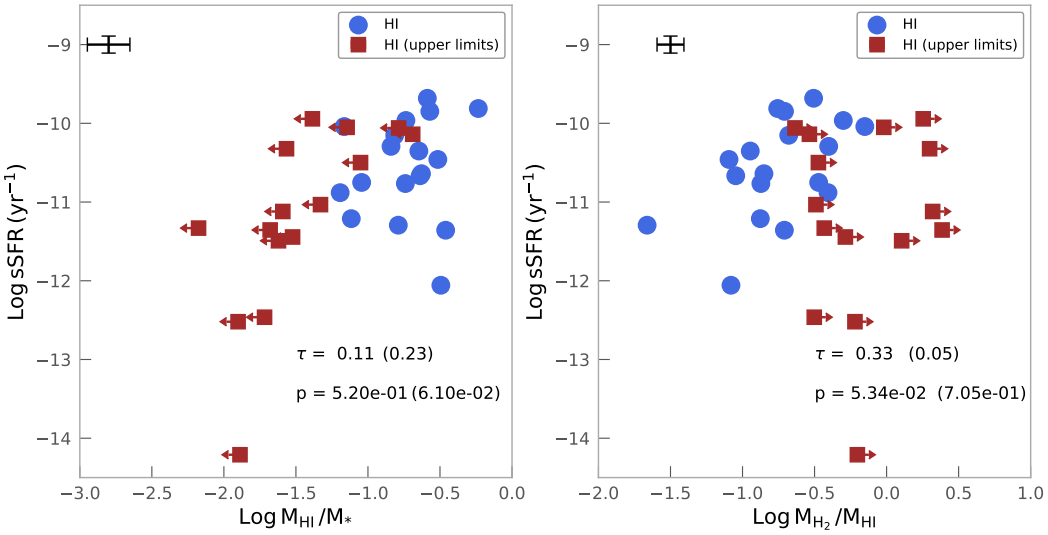

Figure 6. The global sSFR of ALMaQUEST galaxies as a function of the atomic gas fraction (left panel) and the H_2 to HI ratio (right panel). The blue circles and brown squares represent datapoints with and without HI detections, respectively. The black error bars shown in the upper left corners represent the typical uncertainties. The Kendall correlation coefficient (τ) and p-value with/without the upper limits in M_{HI} are shown in the legend (the values in the parenthesis are for the cases when considering the upper limits).

where W_{CO} is the CO line intensity in units of K-km s^{-1} . The metallicity is calculated for spaxels with S/N > 3 for Hα and Hβ and S/N > 2 for [OIII] 5007 and [NII] 6584. For spaxels that do not fulfill the above criteria, we set the metallicity to be the solar value. Although this approach may not be ideal, it offers an approximate view of the level of potential impacts on our derived results. For a given galaxy, we then compute α_{CO} based on the median value of the spaxel-based metallicities. With the varying α_{CO} applied, we find that over the entire ALMaQUEST sample, the difference in the global H_2 mass relative to the original global H_2 mass based on a constant value can be as large as 0.27 dex with an average value of $\sim$ 0.05 and $\sim$ 0.14 dex in method 1 and method 2, respectively. The latter is then combined with the measurement error to calculate the uncertainty of M_{H_2} that is shown in Figure 3. We then proceed with the same analysis and find that despite a systematic offset seen in the M_{H_2} measurement, the varying α_{CO} does not affect any trends in the global results presented in this section.

3.2. *The role of* HI *gas*

While the star formation is closely related to the molecular gas (Wong & Blitz 2002; Gao & Solomon 2004; Wu et al. 2005; de los Reyes & Kennicutt 2019), the atomic gas, particularly the atomic hydrogen, dominates the cold gas mass budget on galactic scales and provides the fuel for future star formation. Although this paper focuses on the influence of molecular gas on star formation, a subset of the ALMaQUEST galaxies have been observed in HI previously (see §2.4), which allows us to investigate the connection between gas and star formation from the atomic hydrogen point of view (e.g. Boselli et al. 2014; Catinella et al. 2018). For example, one can study the dependence of sSFR on the atomic gas fraction (M_{HI}/ M_*), which represents the availability of cold gas reservoir, as well as on the molecular-to-atomic gas ratio (M_{H_2}/M_{HI}), which is related to the efficiency of transforming the atomic gas into the molecular phase. Different from the CO observations, the HI data were taken with single-dish telescopes and have a beam size that well exceeds the optical diameter of the galaxy. The HI mass used here is hence the 'total' HI mass rather than the aperture-matched quantity, such as SFR, M_*, and M_{H_2} used in the previous section.

There are 33 ALMaQUEST galaxies that overlap with the HI-MaNGA (Masters et al. 2019) and ALFALFA (Haynes et al. 2018) observations, of which 18 are detected in HI with S/N > 5. Figure 5 shows their distributions in the SFR vs. M_* plane (blue: HI detected; brown: HI undetected) with respect to the rest 13 ALMaQUEST galaxies without HI observations (green triangles). Proportionally there are fewer high stellar mass galaxies with HI observations (blue + brown symbols) compared to the rest of the ALMaQUEST sample (green symbols). Among the HI sample, galaxies with and without HI detections are distributed similarly, albeit with small sample sizes.

We compute M_{HI}/ M_* and M_{H_2}/M_{HI} for all the 33 galaxies covered by the HI observations and use the upper limits of M_{HI} in the case of non-detection. According to the M_{H_2}/M_{HI} ratios, the 18 HI-detected galaxies are all HI-dominated (with respect to M_{H_2}) systems. In Figure 6 we plot the dependence of sSFR on M_{HI}/ M_* and M_{H_2}/M_{HI} in the left and right panels, respectively. We perform the Kendall correlation analysis for two cases, one only for the 18 galaxies with solid HI detections and the other including the additional 15 galaxies with upper limits. In both cases (with/without upper limits), the dependence on M_{HI}/ M_* and M_{H_2}/M_{HI} are weaker compared to the dependence of sSFR on SFE or f_{H_2} presented in Figure 4, suggesting that sSFR is more linked to the molecular gas budget than to the atomic gas. Nevertheless, it is worth noting that the dependence of sSFR on M_{HI}/ M_* found in our sample is weaker than the results from earlier studies built upon larger samples (Saintonge et al. 2016; Catinella et al. 2018). Furthermore, in our case without upper limits considered, the correlation is slightly stronger in the sSFR vs. M_{H_2}/M_{HI} relation than in the sSFR vs M_{HI}/ M_* relation, whereas the trend is reversed when the upper limits are taken into account. This shows that galaxies without HI detections

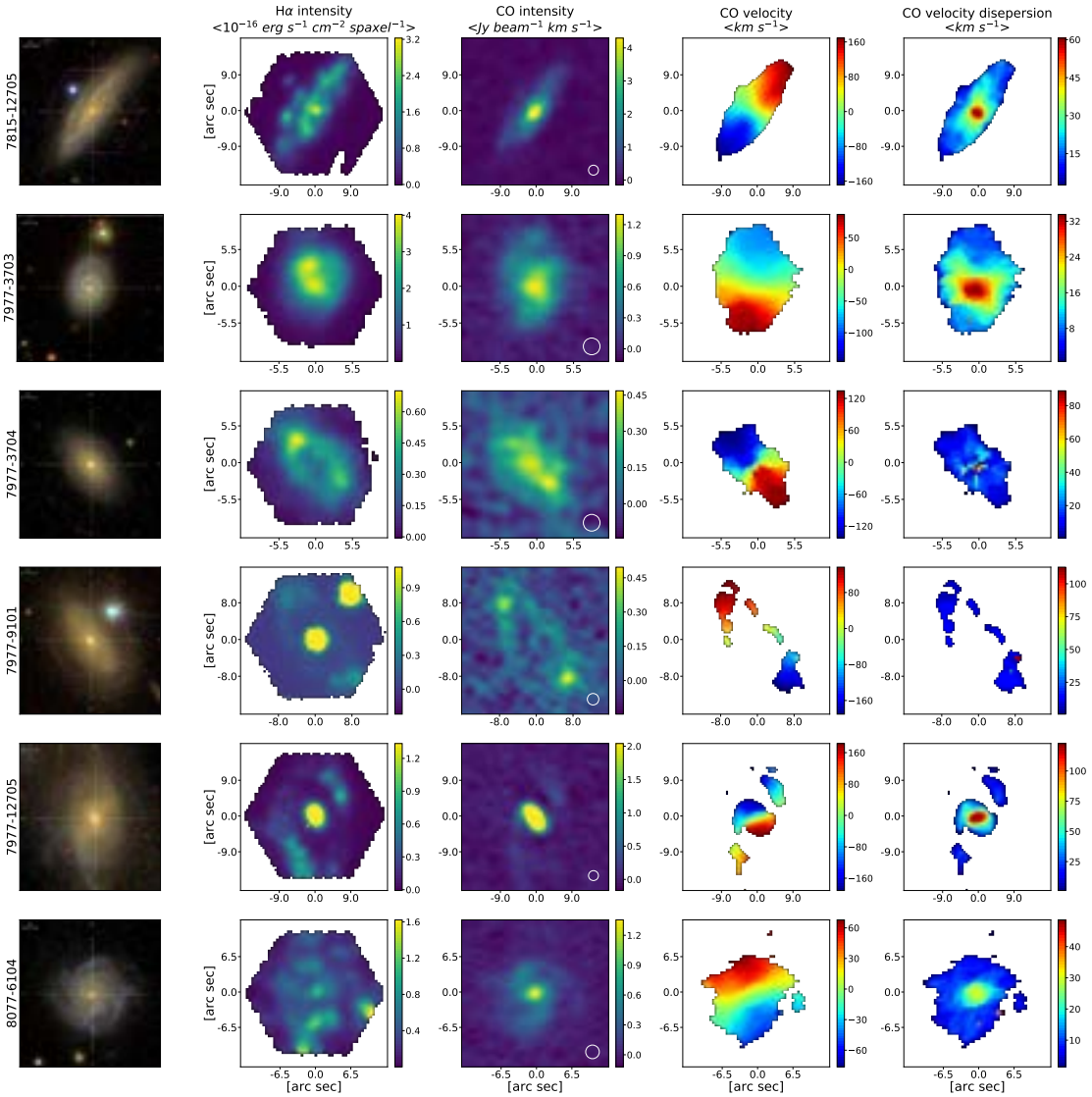

Figure 7. Examples of ALMaQUEST targets. From left to right: SDSS *gri* multicolor images, MaNGA raw Hα intensity (10^{-16} erg s^{-1} cm^{-2} per spaxel) , followed by ALMA ^{12}CO(1-0) intensity (Jy km s^{-1} per beam), velocity (km s^{-1}), and velocity dispersion (km s^{-1}) maps. The white circle in the lower-right corner of the CO panel illustrates the restoring beamsize. A S/N = 3 cut in the ^{12}CO(1-0) intensity is applied when generating the associated velocity fields and dispersion maps. (The complete figure set (8 images) is available in the online journal.)

have a significant impact on the strength of the correlation. Therefore, our results should be taken with caution given that the current ALMaQUEST HI sample size is still limited.

3.3. *Resolved properties of the ALMaQUEST sample*

As our main science goals of the ALMaQUEST survey rely on small scale properties of galaxies, we also constructed spatially resolved intensity and velocity maps for individual galaxies using the procedures described in §2.3. In Figure 7, we show the SDSS optical image, MaNGA Hα intensity, ALMA CO(1-0) integrated intensity, velocity, and velocity dispersion maps for the 46 ALMaQUEST galaxies. In general, it is evident from these maps that the Hα flux does not always trace the CO(1-0) emission. Since Hα is a good tracer of SFR in regions where the photon ionization is dominated by star formation and CO(1-0) mass can be converted into the H_2 mass, the discrepancy in the spatial distributions between Hα and CO(1-0) hence indicates a possible variation of SFE within a galaxy.

To further illustrate this point, we display maps for various physical quantities in Figure 8, including stellar mass surface density Σ_*, H_2 mass surface density (Σ_{H_2}) using a constant α_{CO} = 4.35, extinction-corrected star formation rate surface density (Σ_{SFR}), f_{H_2}, and SFE. Figure 8 shows that neither f_{H_2} nor SFE is a constant across a given galaxy, as also been shown in previous studies of nearby galaxies(e.g. Leroy et al. 2008; Huang & Kauffmann 2015; Utomo et al. 2017; Colombo et al. 2018; Schinnerer et al. 2019; Dey et al. 2019). To quantify the variation, we plot the histograms of sSFR, f_{H_2} and SFE computed on a spaxel-by-spaxel basis for the star-forming spaxels of 46 ALMaQUEST galaxies in Figures 9, 10, and 11, respectively. In the bottom right panel of each figure (Figures 9–11), we show the combined distributions from all the 46 galaxies. When looking at the combined ensemble of spaxels, the distributions of all the three quantities (sSFR, f_{H_2} and SFE) are close to a Gaussian in log space. For the rest panels, the blue and green vertical lines show the median value of the histogram and the globally averaged value

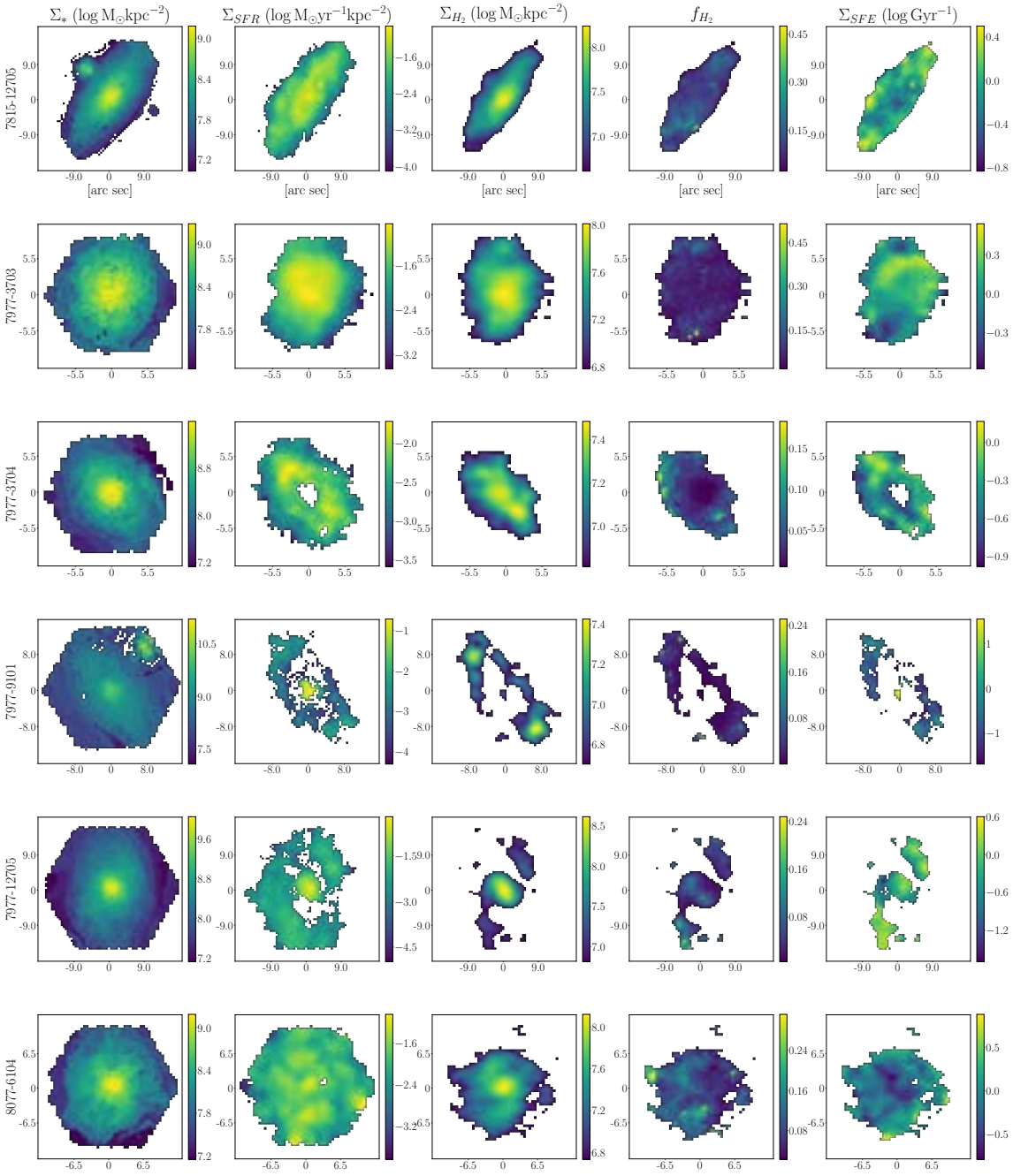

Figure 8. Physical products of the ALMaQUEST sample. From left to right: stellar mass surface density, H_2 mass surface density, SFR surface density, gas fraction, and star fromation efficiency. An S/N > 3 cut in the CO flux is applied. Only spaxels classified as the star-forming regions using the [SII] BPT criteria Kewley et al. (2001, 2006) with an S/N > 3 cut in Hα and Hβ lines and S/N > 2 cut in [OIII] and [SII] lines are shown in the SFR map. (The complete figure set (8 images) is available in the online journal.)

in a given galaxy, respectively. It can be seen that all of these quantities show a large spread (typically spanning 1-2 orders of magnitude within a galaxy), meaning that there is a strong variation even within a single galaxy. Some of the variations are found to be associated with the radial position of the galaxies while some are not (Pan et al. in prep.). Figures 9, 10, and 11 therefore serve as a caveat that using a global value may not properly capture the 'intrinsic' gas content of galaxies (also see Sanchez 2020). Therefore, spatially resolved gas observations are critical in order to characterize the properties of gas and their connections to the star formation activity.

To see if the SFE and $f_{\rm H_2}$ variations are driven by the adoption of a fixed $\alpha_{\rm CO}$, we repeated the same analyses with a metallicity and/or CO intensity-dependent $\alpha_{\rm CO}$ as described in §3.1. While there is a systematic offset (< 0.14 dex) in the resulted SFE and $f_{\rm H_2}$, the overall distributions of the SFE and $f_{\rm H_2}$ remain very similar even if we adopt a varying $\alpha_{\rm CO}$. This suggests that the internal variations seen in the SFE and $f_{\rm H_2}$ are intrinsic and not caused by the choices of $\alpha_{\rm CO}$. In a set of companion papers, we present in detail how the $f_{\rm H_2}$ and

SFE are distributed spatially and which physical parameters are correlated most strongly with the dispersion of f_{H_2} and SFE (Ellison et al. 2020a,b; H.-A. Pan et al. in prep.).

4. ALMAQUEST KEY SCIENCE PAPERS

The combination of spatially resolved stellar populations and emission line measurements from the MaNGA data and the gas properties derived from the ALMA observations enable a variety of kpc-scale investigations. While the primary goal of this paper is to present the main features of the ALMaQUEST survey, here we also highlight some key science applications, which are presented in more detail in a series of ALMaQUEST papers.

4.1. *Kpc-scale scaling relations*

The process of star formation is described by two well-known scaling relations: the so-called 'Schmidt-Kennicutt' relation (SK; Schmidt 1959; Kennicutt 1998), which relates the star formation rate to the underlying gas abundance, and the SFMS (Brinchmann et al. 2004; Noeske et al. 2007; Daddi et al. 2007; Lin et al. 2012; Whitaker et al. 2012; Speagle et al. 2014), a tight correlation between the star formation rate and the stellar mass. While the SK relation can be easily understood as the stars forming within molecular clouds, the origin of the SFMS has been hotly debated (e.g. Kelson 2014; Tacchella et al. 2016; Hsieh et al. 2017; Matthee & Schaye 2019; Morselli et al. 2020; Hani et al. 2020).

With the MaNGA-based measurements of Σ_{SFR} and Σ_* and the ALMA-based Σ_{H_2}, we are able to discuss the relationships among the three quantities on kpc scales. In Lin et al. (2019b), we showed that Σ_{SFR}, Σ_*, and Σ_{H_2} computed for star-forming spaxels of MS galaxies form a linear 3D correlation in log scale. Each pair of these three quantities form a tight correlation, the resolved SFMS (rSFMS; i.e. Σ_{SFR} vs. Σ_*), the resolved SK relation (rSK; i.e. Σ_{SFR} vs. Σ_{H_2}), and the resolved molecular gas main sequence (rMGMS; i. e. Σ_{H_2} vs. Σ_*). By comparing the strength of the correlations and the magnitude of their scatters, we argue that rSFMS is the least fundamental, but rather a natural consequence of the combination of the rSK and rMGMS relations. This result is later supported by Morselli et al. (2020), who study the same scaling relations for five nearby spiral galaxies at 500pc scale, and by Ellison et al. (in prep.) based on a complementary approach applied to the ALMaQUEST sample.

4.2. *What drives the central starburst?*

Previously, it has been shown that local starbursts are preferentially driven by central SFR enhancement (e.g., Morselli et al. 2017; Ellison et al. 2018; Tacconi et al. 2018). However, it remains unclear whether the boost of SFR in central regions is primarily caused by the increased gas fraction or greater star formation efficiency. Pinning down the relative importance between these two scenarios provides key constraints on the physical processes responsible for starbursts. Using the 12 starbursting galaxies from ALMaQUEST, we show in Ellison et al. (2020a) that the central starburst is mainly driven by an elevated SFE. Only one quarter of the sample shows signs of mergers morphologically, indicating that other mechanisms may also produce central starbursts.

4.3. *What regulates the SFR in the star-forming main sequence?*

Recent IFS studies have shown that the tight correlation between global SFR and M_* may in fact originate from the rSFMS at kpc scales (Cano-Díaz et al. 2016; Hsieh et al. 2017; Ellison et al. 2018; Pan et al. 2018; Cano-Díaz et al. 2019, e.g.,). As mentioned in §. 4.1, we further show that the rSFMS is due to a combination of both rSK relation and the rMGMS (Lin et al. 2019b). The rSFMS relation, however, shows a significant scatter ~ 0.25 dex. In Ellison et al. (2020b), we investigate the dependence of the scatter around the rSFMS ($\Delta\Sigma_{SFR}$) on the variation in f_{H_2} and SFE to shed light on the physics regulating the scatter of star forming spaxels around the rSFMS. We found that the change in SFE is the primary cause for $\Delta\Sigma_{SFR}$ while the variation in f_{H_2} is a secondary factor (but see also Dey et al. 2019; Morselli et al. 2020).

4.4. *Gas properties in green valley galaxies*

Our pilot study (Lin et al. 2017) of the CO content of three green valley galaxies suggests that the suppression of SFR in these 'below MS' galaxies can possibly be attributed to the deficit in the gas fraction in the central regions of galaxies, accompanied with a reduction in both the gas fraction and SFE in the disks. With a sample size tenfold larger, we can more rigorously investigate the link between the star formation suppression and the changes in the gas fraction and SFE (L. Lin et al. in prep.). Also, we will characterize the radial distributions of gas fraction and SFE in green valley galaxies compared with those in main sequence galaxies (H.-A. Pan et al. in prep.).

4.5. *The non-universality of resolved scaling relations*

It is now well-established that global relations, such as the SK and SFMS, arise as a result of resolved scale correlations that exist on scales of kpc or less (Wong & Blitz 2002; Bigiel et al. 2008; Schruba et al. 2011; Leroy et al. 2013; Sánchez et al. 2013; Cano-Díaz et al. 2016; González Delgado et al. 2016; Hsieh et al. 2017). The existence of such tight relations on kpc-scales indicates that they may reflect fundamental physical processes that are regulating the distribution of gas and its processing into stars. Testing the variation of these scaling relations, and quantifying the global galactic properties on which they depend will therefore provide insight into the universality of the star formation process and its sensitivity to local environmental conditions. Although past works have investigated the variation of either the rSK relation (e.g. Schruba et al. 2011; Leroy et al. 2013) or the rSFMS (e.g. Abdurro'uf & Akiyama 2017; Pan et al. 2018; Vulcani et al. 2019; Cano-Díaz et al. 2019), the ALMaQUEST sample offers us the opportunity to investigate the variation in all three scaling relations (rSK, rSFMS and rMGMS), as well as study the interplay between them. In Ellison et al. (in prep.) we demonstrate that all three of the resolved scaling relations exhibit significant variation, although this variation is significantly smaller for the rMGMS than for the rSFMS. In Ellison et al. (in prep.) we also demonstrate that the variation in these scaling relations correlates with global galaxy properties such as total stellar mass, Sersic index and sSFR.

4.6. *The cold molecular gas-metallicity relation in MaNGA galaxies*

Several works based on SDSS spectroscopy have demonstrated the existence of a three-dimensional relation between metallicity, stellar mass and SFR (the so-called fundamental metallicity relation or FMR; Lara-López et al. 2010; Mannucci et al. 2010; Salim et al. 2014). Such a relation is naturally predicted by several theoretical models (Davé et

al. 2011; Lagos et al. 2016; Torrey et al. 2019; Trayford & Schaye 2019) as a consequence of a more fundamental link between metallicity, stellar mass and gas content. Models predict that the scatter across the mass-metallicity relation is driven by the competition between phases dominated by gas accretion and metal dilution and subsequent periods of enrichment and low gas fraction. In accordance with the observed FMR, at fixed stellar mass galaxies with higher SFR are predicted to have lower metallicities.

Bothwell et al. (2013) and Brown et al. (2018) studied the role of atomic gas using SDSS spectroscopy matched with HI observations from the ALFALFA survey. Both studies agreed that the FMR is stronger when considering HI gas mass, rather than SFR as the parameter driving the scatter across the mass-metallicity relation. Bothwell et al. (2016a,b) revise the role of gas on the FMR by considering molecular gas. They find that M_{H_2} is the best third parameters for the FMR, and is favoured over both total (atomic + molecular) gas mass or SFE. These findings provide observational confirmation of the importance of gas content, and in particular star-forming molecular gas, in driving the FMR.

Extensions of global scaling relations involving metallicity to resolved kpc-scale regions have been investigated thanks to large IFS surveys, like CALIFA, SAMI and MaNGA. A resolved mass-metallicity relation (Sánchez et al. 2013; Barrera-Ballesteros et al. 2016) is found to exist on kpc scales, and the existence of a secondary dependence of Σ_{SFR} is subject of active research (Barrera-Ballesteros et al. 2016; Belfiore et al. in prep. Also see Sec. 6.4 of Maiolino & Mannucci 2019 for a recent review). With ALMaQUEST we are now able to investigate the importance of Σ_{H_2} in setting the scatter of the resolved mass-metallicity relation and assess its relative importance with respect to Σ_{SFR}.

4.7. *The connection between the Balmer Decrement (BD=Hα/Hβ) and the CO(1-0) line luminosity and total molecular gas mass*

The dust absorption, traced by the reddening and extinction of starlight has been used to estimate the gas content in the Milky Way (e.g. see Bohlin et al. 1978; Lada et al. 1994; Pineda et al. 2010) and more recently in external galaxies (Brinchmann et al. 2013; Concas & Popesso 2019; Piotrowska et al. 2020). In particular, Concas & Popesso (2019) found an empirical relation between the dust extinction, traced by the Balmer Decrement (BD=Hα/Hβ), and the total molecular gas mass in a sample of 222 local galaxies. By following this approach, we will explore whether the local BD-M_{gas} relation and its connection with gas metallicity could be applied at local scales (see also Barrera-Ballesteros et al. 2020), testing a new empirical method to trace the cold gas reservoir in galaxies. The ALMaQUEST sample allows us to extend the study of such relation in galaxies that are above, below and on the SFMS.

5. SUMMARY

We introduce the ALMaQUEST survey, an ALMA program that maps the CO distributions on kpc scales for 46 galaxies selected from the MaNGA IFS survey. Whereas the MaNGA data deliver kpc-scale maps of star formation rate surface density, stellar mass surface density and metallicity, the ALMA observations provide spatially-matched maps of molecular gas. Combined, the ALMA+MaNGA dataset yields a superlative view of star formation in nearby galaxies. The targets of the sample include starburst (SB), main sequence (MS) and green valley (GV) galaxies, allowing one to study the properties of cold ISM, star formation, stellar population, and ionized gas systematically across various galaxy populations.

When looking at the global (aperture-matched) stellar mass, H_2 mass, and star formation rate, it is found that the locations of galaxies with respect to the Schmidt-Kennicutt relation (i.e., the SFE) is closely related to the sSFR (see the middle panel of Figure 3 and the left panel of Figure 4). On the other hand, there exists a large scatter in the H_2 mass vs. stellar mass relation (and hence f_{H_2}) at a given sSFR (see the bottom panel of Figure 3 and the right panel of Figure 4), although galaxies with low sSFR do exhibit significantly lower H_2 mass as opposed to those with high sSFR at a given stellar mass (bottom panel of Figure 3). In general, galaxies with different sSFR are more segregated by their star formation efficiency (SFE) than their molecular gas fractions (f_{H_2}). This is further supported through a correlation analysis, in which we find that sSFR has a slightly stronger dependence on SFE than on f_{H_2}. On the other hand, we show that there is weaker dependence of sSFR on the atomic gas fraction (M_{HI}/ M_*) or the molecular-to-atomic gas fraction (M_{H_2}/M_{HI}) compared to the dependence on SFE and/or f_{H_2}. However, a larger and deeper HI sample is required to draw a robust conclusion.

When comparing the CO and Hα distributions within individual galaxies, we find that these two quantities do not always trace each other. We show that in a given galaxy, there is substantial variation in the sSFR, f_{H_2}, and SFE for regions classified as star-forming spaxels (Figures 9 – 11). Therefore, using a single global measurement may not be able to capture the detailed physics regulating the star formation within a galaxy. In the forthcoming papers, we will investigate in more detail the changes of the sSFR, SFE, and f_{H_2}, as well as the correlations among these three parameters, as a function of various global and local galactic properties.

We thank the anonymous referee for his/her helpful comments. This work is supported by the Academia Sinica under the Career Development Award CDA-107-M03 and the Ministry of Science & Technology of Taiwan under the grant MOST 107-2119-M-001-024 - and 108-2628-M-001 -001 - MY3. SFS thanks CONACYT CB-285080 and FC-2016-01-1916, and PAPIIT-DGAPA-IN100519 (UNAM) grants for supporting this project. RM acknowledges ERC Advanced Grant 695671 'QUENCH' and support by the Science and Technology Facilities Council (STFC). L. Lin and H.-A. Pan thank U. of Victoria for hosting during the visit to work on this project. L. Lin thanks Sophia Y. Dai and Z. Zheng for providing useful suggestions to improve the content of this paper.

The authors would like to thank the staffs of the East-Asia and North-America ALMA ARCs for their support and continuous efforts in helping produce high-quality data products. This paper makes use of the following ALMA data: ADS/JAO.ALMA#2015.1.01225.S, ADS/JAO.ALMA#2017.1.01093.S, ADS/JAO.ALMA#2018.1.00541.S, and ADS/JAO.ALMA#2018.1.00558.S. ALMA is a partnership of ESO (representing its member states), NSF (USA) and NINS (Japan), together with NRC (Canada), MOST and ASIAA (Taiwan), and KASI (Republic of Korea), in cooperation with the Republic of Chile. The Joint ALMA Observatory is operated by ESO, AUI/NRAO and NAOJ.

Funding for the Sloan Digital Sky Survey IV has been provided by the Alfred P. Sloan Foundation, the U.S. Department of Energy Office of Science, and the Participating Institutions. SDSS-IV acknowledges support and resources from the Center for High-Performance Computing at the University of Utah. The SDSS web site is www.sdss.org. SDSS-IV is managed by the Astrophysical Research Consortium for the Participating Institutions of the SDSS Collaboration including the Brazilian Participation Group, the Carnegie Institution for Science, Carnegie Mellon University, the Chilean Participation Group, the French Participation Group, Harvard-Smithsonian Center for Astrophysics, Instituto de Astrofísica de Canarias, The Johns Hopkins University, Kavli Institute for the Physics and Mathematics of the Universe (IPMU) / University of Tokyo, Lawrence Berkeley National Laboratory, Leibniz Institut für Astrophysik Potsdam (AIP), Max-Planck-Institut für Astronomie (MPIA Heidelberg), Max-Planck-Institut für Astrophysik (MPA Garching), Max-Planck-Institut für Extraterrestrische Physik (MPE), National Astronomical Observatory of China, New Mexico State University, New York University, University of Notre Dame, Observatário Nacional / MCTI, The Ohio State University, Pennsylvania State University, Shanghai Astronomical Observatory, United Kingdom Participation Group, Universidad Nacional Autónoma de México, University of Arizona, University of Colorado Boulder, University of Oxford, University of Portsmouth, University of Utah, University of Virginia, University of Washington, University of Wisconsin, Vanderbilt University, and Yale University.

APPENDIX

TESTS ON THE EFFECT OF THE GLOBAL QUANTITY ESTIMATES

The main results concerning the global SFR of the ALMaQUEST sample presented in this work are primarily based on the SFR integrated over the areas classified as 'star-forming' using the [SII] BPT diagnostic (Kewley et al. 2001, 2006). In this section, we test whether our results, specifically for the relation between sSFR and SFE and between sSFR and $f_{\rm H_2}$, are impacted by the choices of integrated areas or not. We repeat our analyses in two cases: a) by summing $\Sigma_{\rm SFR}$ over all spaxels within 1.5 R_e regardless of the BPT types, and b) by summing $\Sigma_{\rm SFR}$ over only the star-forming spaxels (also within 1.5 R_e) classified by the [NII] BPT diagnostic (Kauffmann et al. 2003), to be compared with the results presented in §3.1, which is based on the [SII] BPT method. The caveat of the case (a) is that the SFR could be overestimated because the Hα emissions might be powered by mechanisms other than star formation in non-star forming spaxels.

Figure A1 displays the sSFR vs. SFE (left panel) and sSFR vs. $f_{\rm H_2}$ relations (right panel) when all types of spaxels are used. A moderate correlation ($\tau = 0.56$) with high significance ($\rho < 10^{-7}$) is seen in both panels, suggesting that both SFE and $f_{\rm H_2}$ contribute to the variation of sSFR. In Figure A2 we plot the same relations by integrating only the [NII] BPT-classified star forming spaxels. Similar to Figure 4, a stronger correlation strength ($\tau = 0.78$) is found in the sSFR vs. SFE relation, with respect to the sSFR vs. $f_{\rm H_2}$ relation ($\tau = 0.49$).

In summary, positive correlations are found in both the sSFR–SFE and sSFR–$f_{\rm H_2}$ relations in all the three situations we have tested, including the two cases presented here and the one in §3.1. The strength of the correlation for the sSFR –SFE relation, is found to be more sensitive to the choices of the types of spaxels used for the total SFR calculation, whereas the sSFR–$f_{\rm H_2}$ relation is more stable. Nevertheless, the main conclusion that the sSFR depends on both SFE and $f_{\rm H_2}$ hold in all cases.

REFERENCES

Abdurro'uf, & Akiyama, M. 2017, MNRAS, 469, 2806
Albareti, F. D., Allende Prieto, C., et al. 2017, ApJS accepted, (arXiv:1608.02013)
Barrera-Ballesteros, J. K., Heckman, T. M., Zhu, G. B., et al. 2016, MNRAS, 463, 2513
Barrera-Ballesteros, J. K., Utomo, D., Bolatto, A. D., et al. 2020, MNRAS, 492, 2651
Bigiel, F., Leroy, A., Walter, F., et al. 2008, AJ, 136, 2846
Blanton, M. R., Bershady, M. A., Abolfathi, B., et al. 2017, AJ, 154, 28
Bohlin, R. C., Savage, B. D., & Drake, J. F. 1978, ApJ, 224, 132
Bolatto, A. D., Wolfire, M., & Leroy, A. K. 2013, ARA&A, 51, 207
Bolatto, A. D., Wong, T., Utomo, D., et al. 2017, ApJ, 846, 159
Boselli, A., Cortese, L., Boquien, M., et al. 2014, A&A, 564, A66
Bothwell, M. S., Maiolino, R., Kennicutt, R., et al. 2013, MNRAS, 433, 1425
Bothwell, M. S., Wagg, J., Cicone, C., et al. 2014, MNRAS, 445, 2599
Bothwell, M. S., Maiolino, R., Peng, Y., et al. 2016a, MNRAS, 455, 1156
Bothwell, M. S., Maiolino, R., Cicone, C., et al. 2016b, A&A, 595, A48
Brinchmann, J., Charlot, S., White, S. D. M., et al. 2004, MNRAS, 351, 1151
Brinchmann, J., Charlot, S., Kauffmann, G., et al. 2013, MNRAS, 432, 2112
Brown, T., Cortese, L., Catinella, B., et al. 2018, MNRAS, 473, 1868
Bundy, K., Bershady, M. A., Law, D. R., et al. 2015, ApJ, 798, 7
Cano-Díaz, M., Sánchez, S. F., Zibetti, S., et al. 2016, ApJ, 821, L26
Cano-Díaz, M., Ávila-Reese, V., Sánchez, S. F., et al. 2019, MNRAS, 1830
Cardelli, J. A., Clayton, G. C., & Mathis, J. S. 1989, ApJ, 345, 245
Catinella, B., Saintonge, A., Janowiecki, S., et al. 2018, MNRAS, 476, 875
Chevance, M., Kruijssen, J. M. D., Hygate, A. P. S., et al. 2020, MNRAS, 493, 2872
Cicone, C., Bothwell, M., Wagg, J., et al. 2017, A&A, 604, A53
Colombo, D., Kalinova, V., Utomo, D., et al. 2018, MNRAS, 475, 1791
Concas, A., & Popesso, P. 2019, MNRAS, 486, L91
Daddi, E., Dickinson, M., Morrison, G., et al. 2007, ApJ, 670, 156
Davé, R., Finlator, K., & Oppenheimer, B. D. 2011, MNRAS, 416, 1354
de los Reyes, M. A. C., & Kennicutt, R. C. 2019, ApJ, 872, 16
Dey, B., Rosolowsky, E., Cao, Y., et al. 2019, MNRAS, 488, 1926
Dressler, A. 1980, ApJ, 236, 351
Drory, N., MacDonald, N., Bershady, M. A., et al. 2015, AJ, 149, 77
Elbaz, D., Daddi, E., Le Borgne, D., et al. 2007, A&A, 468, 33
Ellison, S. L., Sánchez, S. F., Ibarra-Medel, H., et al. 2018, MNRAS, 474, 2039
Ellison, S. L., Thorp, M. D., Pan, H.-A., et al. 2020a, MNRAS, 492, 6027
Ellison, S. L., Thorp, M. D., Lin, L., et al. 2020b, MNRAS, 493, L39
Gao, Y., & Solomon, P. M. 2004, ApJ, 606, 271
González Delgado, R. M., Pérez, E., Cid Fernandes, R., et al. 2014, A&A, 562, A47
González Delgado, R. M., Cid Fernandes, R., Pérez, E., et al. 2016, A&A, 590, A44
Gunn, J. E., Siegmund, W. A., Mannery, E. J., et al. 2006, AJ, 131, 2332
Hani, M. H., Hayward, C. C., Orr, M. E., et al. 2020, MNRAS, 493, L87
Haynes, M. P., Giovanelli, R., Kent, B. R., et al. 2018, ApJ, 861, 49
Hsieh, B. C., Lin, L., Lin, J. H., et al. 2017, ApJ, 851, L24
Huang, M.-L., & Kauffmann, G. 2014, MNRAS, 443, 1329
Huang, M.-L., & Kauffmann, G. 2015, MNRAS, 450, 1375
Isbell, J. W., Xue, R., & Fu, H. 2018, ApJ, 869, L37
Jian, H.-Y., Lin, L., Oguri, M., et al. 2018, PASJ, 70, S23
Kauffmann, G., Heckman, T. M., Tremonti, C., et al. 2003,
Kelson, D. D. 2014, arXiv e-prints, arXiv:1406.5191
Kennicutt, R. C., Jr. 1998, ApJ, 498, 541
Kewley, L. J., Dopita, M. A., Sutherland, R. S., Heisler, C. A., & Trevena, J. 2001, ApJ, 556, 121

Table 1
ALMaQUEST Targets and CO(1-0) Sensitivities

Plate-IFU	RA (deg)	DEC (deg)	MaNGA redshift	$\sigma_{CO}^{(a)}$ (Jy beam^{-1} km s^{-1})
7815-12705	318.990448	9.543076	0.029550	0.0591
7977-3703	333.052032	12.205191	0.027817	0.0355
7977-3704	332.798737	11.800733	0.027245	0.0487
7977-9101	331.122894	12.442626	0.026562	0.0472
7977-12705	332.892853	11.795929	0.027236	0.0493
8077-6104	42.032784	-0.752316	0.046014	0.0278
8077-9101	41.643112	-0.843537	0.043226	0.0365
8078-6103	42.416542	-0.069851	0.028593	0.0919
8078-12701	40.880466	0.306821	0.026977	0.0566
8081-3704	49.821442	-0.969631	0.054004	0.0699
8081-6102	49.940136	-0.077189	0.037189	0.0461
8081-9101	47.772182	-0.546538	0.028460	0.0470
8081-9102	49.845692	0.823470	0.034069	0.0862
8081-12703	50.391369	-0.178368	0.025583	0.0378
8082-6103	49.782173	0.955959	0.024157	0.0203
8082-12701	48.896458	-1.016286	0.027026	0.0279
8082-12704	49.949562	-0.221145	0.132144	0.0300
8083-6101	50.504082	-1.053930	0.026766	0.0559
8083-9101	50.138412	-0.339960	0.038470	0.1030
8083-12702	50.245415	-0.367683	0.021040	0.0409
8084-3702	50.636642	-0.001213	0.022061	0.0275
8084-6103	50.741676	0.054137	0.035927	0.0498
8084-12705	51.027115	-1.057859	0.025446	0.0452
8086-9101	57.242985	-0.521120	0.040035	0.0439
8155-6101	53.814114	-1.228609	0.037403	0.2599
8155-6102	52.621368	0.752068	0.030814	0.0406
8156-3701	55.592297	-0.583196	0.052726	0.0246
8241-3703	126.461189	18.166689	0.029113	0.0307
8241-3704	126.568909	17.362452	0.066173	0.0411
8450-6102	171.748840	21.141676	0.041996	0.0194
8615-3703	320.826416	1.254980	0.018452	0.0422
8615-9101	319.919739	0.120941	0.033459	0.0297
8615-12702	320.159454	1.047277	0.020947	0.0248
8616-6104	322.980530	0.213767	0.054257	0.0249
8616-9102	322.749451	-0.000594	0.030386	0.0479
8616-12702	322.306061	-0.294765	0.030831	0.0209
8618-9102	319.271454	9.972303	0.043337	0.0391
8623-6104	311.780975	0.300461	0.097041	0.0276
8623-12702	310.217072	0.652804	0.026910	0.0698
8655-3701	356.751831	-0.447387	0.071489	0.0535
8655-9102	358.221924	-0.382447	0.045050	0.0206
8655-12705	357.651733	-1.128090	0.045568	0.0201
8728-3701	57.699028	-7.028787	0.028327	0.0701
8950-12705	194.733139	27.833445	0.025277	0.0545
8952-6104	204.933975	27.776474	0.028433	0.0386
8952-12701	204.683838	26.328539	0.028563	0.0393

Note. — $^{(a)}$The 1σ sensitivity of the integrated ALMA CO intensity maps (see §2.3), calculated using the spectral window shown as the yellow area in Figure 2.

Kewley, L. J., Groves, B., Kauffmann, G., & Heckman, T. 2006, MNRAS, 372, 961
Koyama, Y., Smail, I., Kurk, J., et al. 2013, MNRAS, 434, 423
Lada, C. J., Lada, E. A., Clemens, D. P., et al. 1994, ApJ, 429, 694
Lagos, C. del P., Theuns, T., Schaye, J., et al. 2016, MNRAS, 459, 2632
Lara-López, M. A., Cepa, J., Bongiovanni, A., et al. 2010, A&A, 521, L53
Law, D. R., Yan, R., Bershady, M. A., et al. 2015, AJ, 150, 19
Law, D. R., Cherinka, B., Yan, R., et al. 2016, AJ, 152, 83
Leroy, A. K., Walter, F., Brinks, E., et al. 2008, AJ, 136, 2782
Leroy, A. K., Walter, F., Sandstrom, K., et al. 2013, AJ, 146, 19
Li, C., Wang, E., Lin, L., et al. 2015, ApJ, 804, 125
Lin, L., Dickinson, M., Jian, H.-Y., et al. 2012, ApJ, 756, 71
Lin, L., Jian, H.-Y., Foucaud, S., et al. 2014, ApJ, 782, 33
Lin, L., Belfiore, F., Pan, H.-A., et al. 2017, ApJ, 851, 18
Lin, L., Bau-Ching Hsieh, Pan, H.-A., et al. 2019a, ApJ, 872, 50
Lin, L., Pan, H.-A., Ellison, S. L., et al. 2019b, ApJ, 884, L33
Maiolino, R., & Mannucci, F. 2019, A&A Rev., 27, 3
Mannucci, F., Cresci, G., Maiolino, R., et al. 2010, MNRAS, 408, 2115
Narayanan, D., Krumholz, M. R., Ostriker, E. C., et al. 2012, MNRAS, 421, 3127
Masters, K. L., Stark, D. V., Pace, Z. J., et al. 2019, MNRAS, 488, 3396
Matthee, J., & Schaye, J. 2019, MNRAS, 484, 915
McMullin, J. P., Waters, B., Schiebel, D., Young, W., & Golap, K. 2007, Astronomical Data Analysis Software and Systems XVI, 376, 127
Medling, A. M., Cortese, L., Croom, S. M., et al. 2018, MNRAS, 475, 5194
Morselli, L., Popesso, P., Erfanianfar, G., et al. 2017, A&A, 597, A97
Morselli, L., Rodighiero, G., Enia, A., et al. 2020, arXiv e-prints, arXiv:2003.02861
Noeske, K. G., Faber, S. M., Weiner, B. J., et al. 2007, ApJ, 660, L47
Pan, H.-A., Lin, L., Hsieh, B.-C., et al. 2018, ApJ, 854, 159
Pettini, M., & Pagel, B. E. J. 2004, MNRAS, 348, L59
Pineda, J. L., Goldsmith, P. F., Chapman, N., et al. 2010, ApJ, 721, 686
Piotrowska, J. M., Bluck, A. F. L., Maiolino, R., et al. 2020, MNRAS, 492, L6
Rahmani, S., Lianou, S., & Barmby, P. 2016, MNRAS, 456, 4128
Saintonge, A., Kauffmann, G., Kramer, C., et al. 2011, MNRAS, 415, 32
Saintonge, A., Catinella, B., Cortese, L., et al. 2016, MNRAS, 462, 1749
Saintonge, A., Catinella, B., Tacconi, L. J., et al. 2017, ApJS, 233, 22
Salim, S., Lee, J. C., Ly, C., et al. 2014, ApJ, 797, 126
Sánchez, S. F., Rosales-Ortega, F. F., Jungwiert, B., et al. 2013, A&A, 554, A58
Sánchez, S. F., Pérez, E., Sánchez-Blázquez, P., et al. 2016, RMxAA, 52, 21
Sánchez, S. F., Pérez, E., Sánchez-Blázquez, P., et al. 2016b, RMxAA, 52, 171

Table 2
Properties of ALMaQUEST Galaxies Measured within $1.5R_e$

Plateifu	Area (kpc^2)	$\log_{10}(M_*/M_\odot)$	$\log_{10}(\frac{SFR}{M_\odot\,yr^{-1}})^{(a)}$	$S_{CO(1-0)}$ (Jy km s^{-1})	$\log_{10}(M_{H_2}/M_\odot)^{(b)}$	$\log_{10}(\frac{SSFR}{yr^{-1}})$	$\log_{10}(\frac{SFE}{yr^{-1}})$	$\log_{10} f_{H_2}$
7815-12705	102.58	10.77	0.80	31.76 ± 0.19	9.728 ± 0.003	-9.96	-8.93	-1.04
7977-3703	45.27	10.43	0.39	8.86 ± 0.04	9.119 ± 0.002	-10.04	-8.72	-1.31
7977-3704	27.34	10.45	-0.59	2.96 ± 0.02	8.626 ± 0.003	-11.03	-9.21	-1.82
7977-9101	68.88	11.20	-0.14	2.80 ± 0.01	8.587 ± 0.002	-11.33	-8.72	-2.61
7977-12705	124.02	11.02	0.66	18.62 ± 0.16	9.422 ± 0.004	-10.35	-8.76	-1.59
8077-6104	294.49	10.75	0.61	8.07 ± 0.03	9.524 ± 0.002	-10.14	-8.91	-1.23
8077-9101	52.70	10.42	-0.08	2.17 ± 0.02	8.897 ± 0.003	-10.50	-8.97	-1.52
8078-6103	69.77	10.80	0.51	23.16 ± 0.12	9.558 ± 0.002	-10.29	-9.05	-1.24
8078-12701	180.47	11.12	0.37	29.18 ± 0.15	9.608 ± 0.002	-10.75	-9.23	-1.52
8081-3704	89.82	10.33	0.91	2.73 ± 0.01	9.195 ± 0.002	-9.42	-8.28	-1.13
8081-6102	93.51	10.95	-1.52	1.99 ± 0.02	8.728 ± 0.004	-12.46	-10.24	-2.22
8081-9101	78.58	10.73	0.41	18.89 ± 0.15	9.469 ± 0.003	-10.32	-9.06	-1.27
8081-9102	67.68	10.81	0.17	9.78 ± 0.08	9.335 ± 0.003	-10.64	-9.16	-1.48
8081-12703	67.46	10.51	-0.98	7.92 ± 0.09	8.995 ± 0.005	-11.49	-9.98	-1.52
8082-6103	47.42	10.20	0.35	7.47 ± 0.02	8.920 ± 0.001	-9.85	-8.57	-1.28
8082-12701	150.88	10.53	0.07	6.00 ± 0.02	8.925 ± 0.001	-10.46	-8.85	-1.61
8082-12704	1442.02	11.66	-0.31	5.22 ± 0.03	10.271 ± 0.002	-11.97	-10.58	-1.39
8083-6101	121.71	10.57	-0.79	18.23 ± 0.18	9.400 ± 0.004	-11.36	-10.19	-1.17
8083-9101	153.03	11.30	0.42	17.48 ± 0.23	9.702 ± 0.006	-10.88	-9.28	-1.60
8083-12702	93.19	11.24	0.51	34.22 ± 0.14	9.468 ± 0.002	-10.73	-8.96	-1.78
8084-3702	29.16	10.43	0.48	21.34 ± 0.13	9.294 ± 0.003	-9.94	-8.81	-1.13
8084-6103	54.86	10.71	-0.65	10.29 ± 0.11	9.412 ± 0.005	-11.36	-10.06	-1.29
8084-12705	58.34	10.60	-0.06	6.70 ± 0.03	8.919 ± 0.002	-10.67	-8.98	-1.69
8086-9101	133.88	11.12	-0.09	4.35 ± 0.02	9.133 ± 0.002	-11.21	-9.22	-1.99
8155-6101	151.71	11.18	-3.03	4.52 ± 0.17	9.087 ± 0.017	-14.21	-12.12	-2.09
8155-6102	120.80	10.38	0.33	9.55 ± 0.03	9.243 ± 0.001	-10.05	-8.91	-1.14
8156-3701	118.32	10.27	0.81	1.58 ± 0.01	8.934 ± 0.002	-9.46	-8.12	-1.33
8241-3703	70.70	10.23	0.23	4.14 ± 0.02	8.830 ± 0.002	-9.99	-8.60	-1.40
8241-3704	353.02	11.06	1.22	12.62 ± 0.09	10.039 ± 0.003	-9.84	-8.82	-1.02
8450-6102	152.67	10.31	0.63	4.75 ± 0.02	9.213 ± 0.002	-9.68	-8.59	-1.09
8615-3703	11.00	10.23	0.42	23.18 ± 0.22	9.175 ± 0.004	-9.81	-8.75	-1.06
8615-9101	83.07	10.78	0.01	6.77 ± 0.03	9.166 ± 0.002	-10.77	-9.15	-1.61
8615-12702	137.43	10.21	0.10	5.27 ± 0.02	8.645 ± 0.001	-10.10	-8.54	-1.56
8616-6104	226.96	10.90	0.21	4.26 ± 0.02	9.392 ± 0.002	-10.69	-9.18	-1.50
8616-9102	149.27	10.44	0.62	15.68 ± 0.07	9.446 ± 0.002	-9.81	-8.82	-0.99
8616-12702	271.43	10.93	-0.36	1.66 ± 0.01	8.483 ± 0.002	-11.29	-8.84	-2.45
8618-9102	65.61	10.47	0.42	5.52 ± 0.04	9.306 ± 0.003	-10.05	-8.89	-1.16
8623-6104	283.83	11.34	1.20	6.32 ± 0.04	10.077 ± 0.003	-10.14	-8.88	-1.27
8623-12702	125.06	10.96	0.11	25.97 ± 0.14	9.561 ± 0.002	-10.86	-9.45	-1.40
8655-3701	197.71	11.27	1.16	25.68 ± 0.27	10.416 ± 0.005	-10.11	-9.26	-0.85
8655-9102	93.75	10.31	0.25	1.93 ± 0.01	8.884 ± 0.002	-10.06	-8.64	-1.42
8655-12705	188.39	10.51	-1.55	2.11 ± 0.01	8.931 ± 0.003	-12.06	-10.48	-1.57
8728-3701	51.92	10.85	-1.67	3.51 ± 0.04	8.730 ± 0.005	-12.52	-10.40	-2.12
8950-12705	42.46	10.73	-0.39	23.41 ± 0.23	9.460 ± 0.004	-11.12	-9.85	-1.27
8952-6104	132.94	10.60	0.45	8.28 ± 0.03	9.111 ± 0.001	-10.15	-8.66	-1.49
8952-12701	127.50	10.78	-0.66	6.06 ± 0.04	8.974 ± 0.003	-11.44	-9.63	-1.81

Note. — [a] Only spaxels classified as star-forming are included. [b] The uncertainty listed here only refers to the measurement error, not yet including the uncertainty in the CO-to-H_2 conversion factor.

Sánchez, S. F., Avila-Reese, V., Hernandez-Toledo, H., et al. 2018, RMxAA, 54, 217
Sánchez, S. F. 2020, ARA&A, in press
Sargent, M. T., Daddi, E., Béthermin, M., et al. 2014, ApJ, 793, 19
Schinnerer, E., Hughes, A., Leroy, A., et al. 2019, ApJ, 887, 49
Schmidt, M. 1959, ApJ, 129, 243
Schruba, A., Leroy, A. K., Walter, F., et al. 2011, AJ, 142, 37
Smee, S. A., Gunn, J. E., Uomoto, A., et al. 2013, AJ, 146, 32
Speagle, J. S., Steinhardt, C. L., Capak, P. L., & Silverman, J. D. 2014, ApJS, 214, 15
Sun, J., Leroy, A. K., Ostriker, E. C., et al. 2020, ApJ, 892, 148
Tacchella, S., Carollo, C. M., Renzini, A., et al. 2015, Science, 348, 314
Tacchella, S., Dekel, A., Carollo, C. M., et al. 2016, MNRAS, 457, 2790
Tacconi, L. J., Neri, R., Genzel, R., et al. 2013, ApJ, 768, 74
Tacconi, L. J., Genzel, R., Saintonge, A., et al. 2018, ApJ, 853, 179
Torrey, P., Vogelsberger, M., Marinacci, F., et al. 2019, MNRAS, 484, 5587
Trayford, J. W., & Schaye, J. 2019, MNRAS, 485, 5715
Usero, A., Leroy, A. K., Walter, F., et al. 2015, AJ, 150, 115
Utomo, D., Bolatto, A. D., Wong, T., et al. 2017, ApJ, 849, 26
Vulcani, B., Poggianti, B. M., Moretti, A., et al. 2019, arXiv e-prints, arXiv:1907.00976
Wake, D. A., Bundy, K., Diamond-Stanic, A. M., et al. 2017, AJ, 154, 86
Wang, E., Lilly, S. J., Pezzulli, G., et al. 2019, ApJ, 877, 132
Whitaker, K. E., van Dokkum, P. G., Brammer, G., et al. 2012, ApJ, 754, L29
Wong, T., & Blitz, L. 2002, ApJ, 569, 157
Wu, J., Evans, N. J., Gao, Y., et al. 2005, ApJ, 635, L173
Wuyts, S., Förster Schreiber, N. M., Nelson, E. J., et al. 2013, ApJ, 779, 135
Yan, R., Tremonti, C., Bershady, M. A., et al. 2016a, AJ, 151, 8
Yan, R., Bundy, K., Law, D. R., et al. 2016b, AJ, 152, 197

Table 3
Properties of ALMaQUEST Galaxies Measured within the MaNGA Bundle Coverage

Plateifu	$\log_{10}(M_*/M_\odot)$	$\log_{10}(\frac{SFR}{M_\odot yr^{-1}})^{(a)}$	$S_{CO(1-0)}$ (Jy km s^{-1})	$\log_{10}(M_{H_2}/M_\odot)^{(b)}$	$\log_{10}(\frac{SSFR}{yr^{-1}})$	$\log_{10}(\frac{SFE}{yr^{-1}})$	$\log_{10} f_{H_2}$
7815-12705	10.82	0.84	31.23 ± 0.19	9.720 ± 0.003	-9.98	-8.88	-1.10
7977-3703	10.50	0.42	9.90 ± 0.04	9.167 ± 0.002	-10.08	-8.74	-1.34
7977-3704	10.54	-0.42	3.82 ± 0.02	8.737 ± 0.002	-10.95	-9.15	-1.80
7977-9101	11.27	-0.09	4.50 ± 0.02	8.794 ± 0.002	-11.36	-8.88	-2.47
7977-12705	11.05	0.70	18.27 ± 0.16	9.414 ± 0.004	-10.35	-8.71	-1.64
8077-6104	10.78	0.69	8.20 ± 0.03	9.531 ± 0.002	-10.09	-8.84	-1.25
8077-9101	10.55	-0.02	2.23 ± 0.02	8.907 ± 0.003	-10.57	-8.93	-1.65
8078-6103	10.88	0.65	26.91 ± 0.12	9.623 ± 0.002	-10.23	-8.97	-1.26
8078-12701	11.15	0.42	26.35 ± 0.15	9.564 ± 0.002	-10.73	-9.15	-1.58
8081-3704	10.54	1.07	3.18 ± 0.01	9.261 ± 0.002	-9.47	-8.19	-1.28
8081-6102	11.03	-1.20	1.97 ± 0.02	8.722 ± 0.004	-12.22	-9.92	-2.30
8081-9101	10.82	0.42	18.10 ± 0.15	9.450 ± 0.004	-10.40	-9.03	-1.37
8081-9102	10.89	0.26	8.73 ± 0.08	9.286 ± 0.004	-10.63	-9.03	-1.60
8081-12703	10.55	-0.98	6.89 ± 0.09	8.934 ± 0.006	-11.53	-9.91	-1.62
8082-6103	10.30	0.41	7.82 ± 0.02	8.940 ± 0.001	-9.90	-8.53	-1.36
8082-12701	10.59	0.16	5.73 ± 0.02	8.905 ± 0.001	-10.43	-8.75	-1.68
8082-12704	11.76	-0.30	4.63 ± 0.03	10.219 ± 0.003	-12.06	-10.52	-1.54
8083-6101	10.58	-0.80	15.43 ± 0.18	9.327 ± 0.005	-11.38	-10.12	-1.26
8083-9101	11.37	0.50	15.67 ± 0.23	9.655 ± 0.006	-10.87	-9.15	-1.71
8083-12702	11.30	0.74	42.09 ± 0.14	9.558 ± 0.001	-10.56	-8.82	-1.74
8084-3702	10.46	0.50	21.79 ± 0.13	9.303 ± 0.003	-9.96	-8.80	-1.16
8084-6103	10.79	-0.65	10.01 ± 0.11	9.400 ± 0.005	-11.44	-10.05	-1.39
8084-12705	10.65	0.00	5.83 ± 0.04	8.858 ± 0.003	-10.65	-8.86	-1.79
8086-9101	11.22	0.08	5.19 ± 0.02	9.209 ± 0.002	-11.14	-9.13	-2.01
8155-6101	11.22	-3.03	4.84 ± 0.19	9.116 ± 0.017	-14.26	-12.15	-2.11
8155-6102	10.43	0.40	10.38 ± 0.03	9.279 ± 0.001	-10.03	-8.88	-1.15
8156-3701	10.41	0.91	1.94 ± 0.01	9.024 ± 0.002	-9.50	-8.11	-1.38
8241-3703	10.26	0.27	4.23 ± 0.02	8.838 ± 0.002	-9.99	-8.57	-1.42
8241-3704	11.09	1.25	12.58 ± 0.09	10.037 ± 0.003	-9.83	-8.78	-1.05
8450-6102	10.39	0.66	4.96 ± 0.02	9.232 ± 0.002	-9.72	-8.57	-1.15
8615-3703	10.34	0.44	29.80 ± 0.23	9.284 ± 0.003	-9.90	-8.84	-1.06
8615-9101	10.84	0.05	6.13 ± 0.03	9.123 ± 0.002	-10.79	-9.08	-1.72
8615-12702	10.23	0.09	4.32 ± 0.02	8.559 ± 0.002	-10.14	-8.47	-1.67
8616-6104	10.96	0.23	4.14 ± 0.02	9.379 ± 0.002	-10.73	-9.15	-1.58
8616-9102	10.47	0.68	15.04 ± 0.07	9.428 ± 0.002	-9.79	-8.75	-1.04
8616-12702	10.97	-0.34	1.43 ± 0.01	8.416 ± 0.003	-11.31	-8.75	-2.56
8618-9102	10.57	0.46	5.18 ± 0.04	9.278 ± 0.003	-10.11	-8.82	-1.29
8623-6104	11.53	1.29	7.12 ± 0.04	10.129 ± 0.002	-10.24	-8.84	-1.40
8623-12702	11.00	0.11	22.30 ± 0.14	9.495 ± 0.003	-10.89	-9.39	-1.51
8655-3701	11.33	1.16	26.53 ± 0.27	10.430 ± 0.004	-10.17	-9.27	-0.90
8655-9102	10.43	0.27	1.70 ± 0.01	8.829 ± 0.002	-10.15	-8.55	-1.60
8655-12705	10.55	-1.54	1.51 ± 0.01	8.786 ± 0.004	-12.09	-10.33	-1.76
8728-3701	10.88	-1.67	3.34 ± 0.04	8.709 ± 0.005	-12.55	-10.38	-2.17
8950-12705	11.16	-0.38	22.77 ± 0.23	9.448 ± 0.004	-11.54	-9.83	-1.72
8952-6104	10.62	0.46	8.40 ± 0.03	9.117 ± 0.001	-10.16	-8.65	-1.51
8952-12701	10.86	-0.66	5.25 ± 0.04	8.912 ± 0.004	-11.52	-9.57	-1.94

Note. — [(a)] Only spaxels classified as star-forming are included. [(b)] The uncertainty listed here only refers to the measurement error, not yet including the uncertainty in the CO-to-H_2 conversion factor.

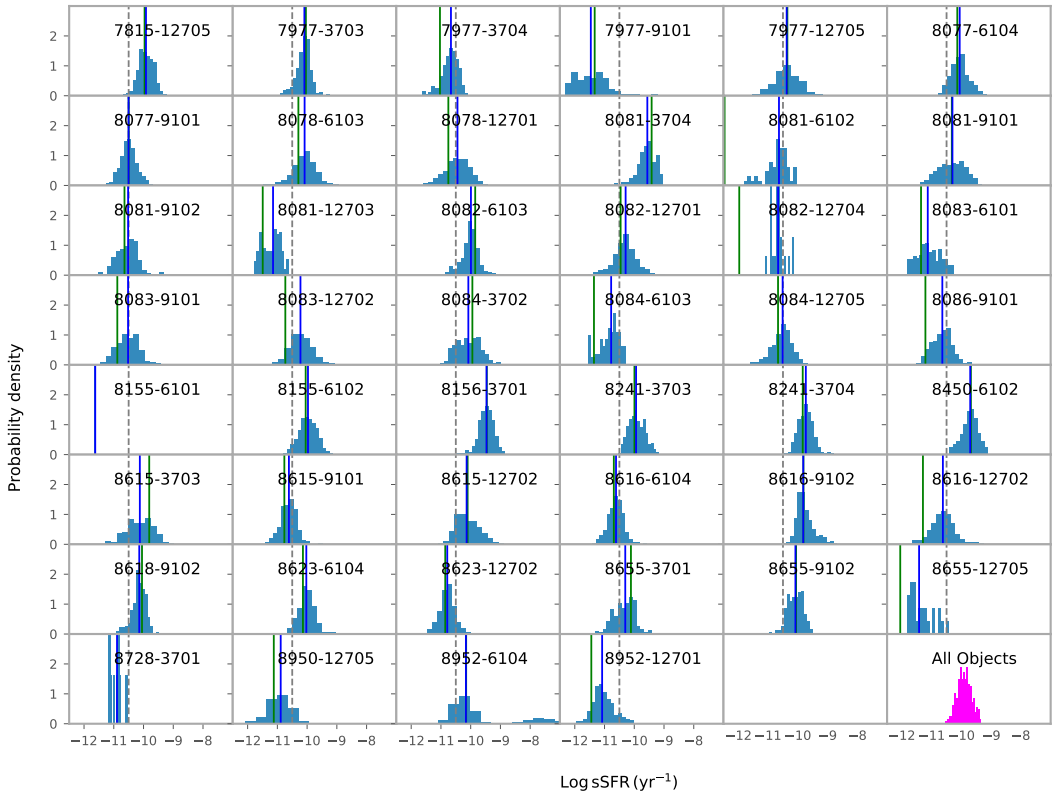

Figure 9. Distributions of sSFR calculated on a spaxel-by-spaxel basis for 46 ALMaQUEST galaxies using only star-forming spaxels. The blue and green vertical lines represent the median of the histogram and the globally averaged value (within $1.5R_e$) of individual galaxy, respectively. The gray dashed lines represent the constant value of $\mathrm{Log_{10}sSFR\ (yr^{-1})}$ = -10.5 as a reference line. In some galaxies (e.g., 8082-12704), the global averaged value is very different to the median value of the histogram because the fraction of star-forming spaxels is low. The last panel shows the distribution of spaxels from all 46 galaxies.

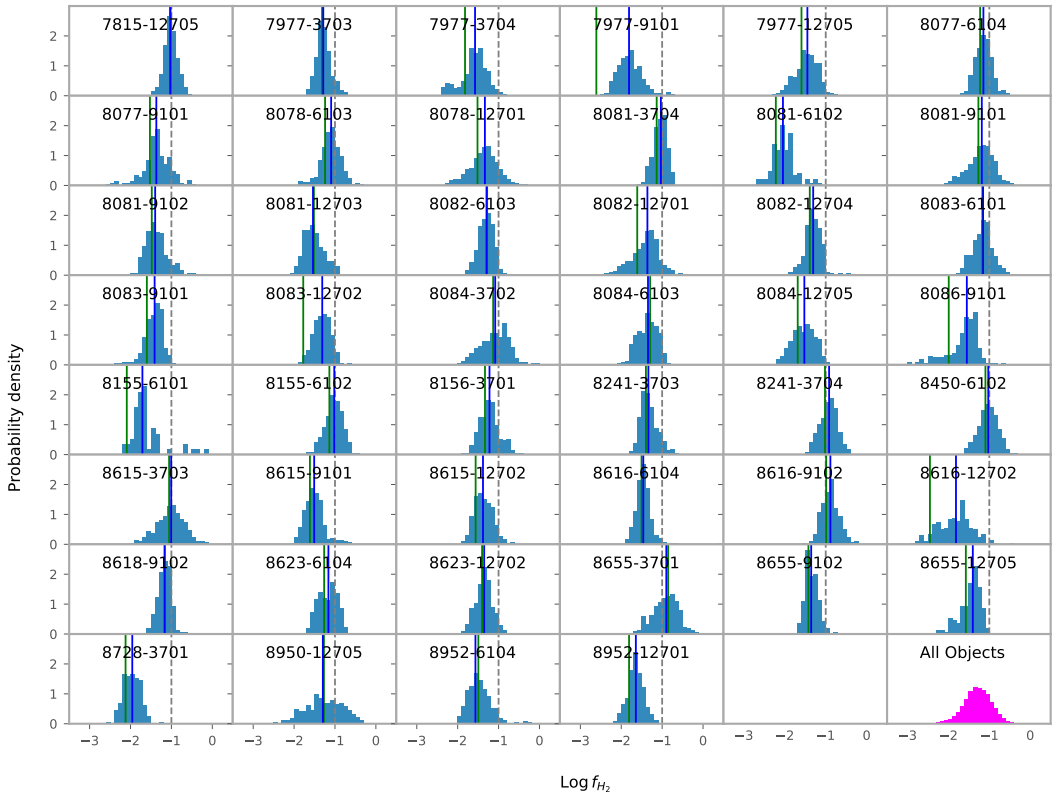

Figure 10. Distributions of $f_{\mathrm{H_2}}$ calculated on a spaxel-by-spaxel basis for 46 ALMaQUEST galaxies. The blue and green vertical lines represent the median of the histogram and the globally averaged value (within $1.5R_e$) of individual galaxy, respectively. The gray dashed lines represent the constant value of $\mathrm{Log}_{10} f_{\mathrm{gas}}$ = -1 as a reference line. The histograms only represent spaxels with CO detections. In some galaxies (e.g., 8086-9101), the global averaged value is very different to the median value of the histogram because there is a significant fraction of spaxels without CO measurements. The last panel shows the distribution of spaxels from all 46 galaxies.

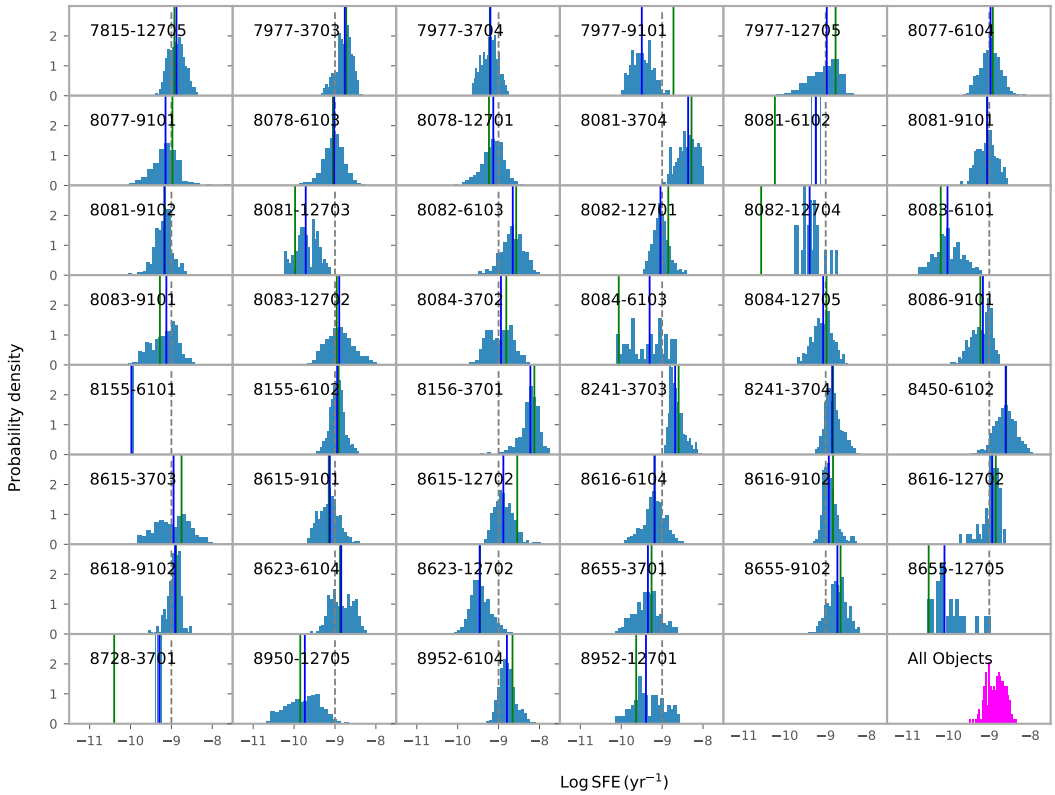

Figure 11. Distributions of SFE calculated on a spaxel-by-spaxel basis for 46 ALMaQUEST galaxies using only star-forming spaxels. The blue and green vertical lines represent the median of the histogram and the globally averaged value (within 1.5R_e) of individual galaxy, respectively. The gray dashed lines represent the constant value of $\mathrm{Log_{10}SFE\ (yr^{-1})}$ = -9 as a reference line. The last panel shows the distribution of spaxels from all 46 galaxies.

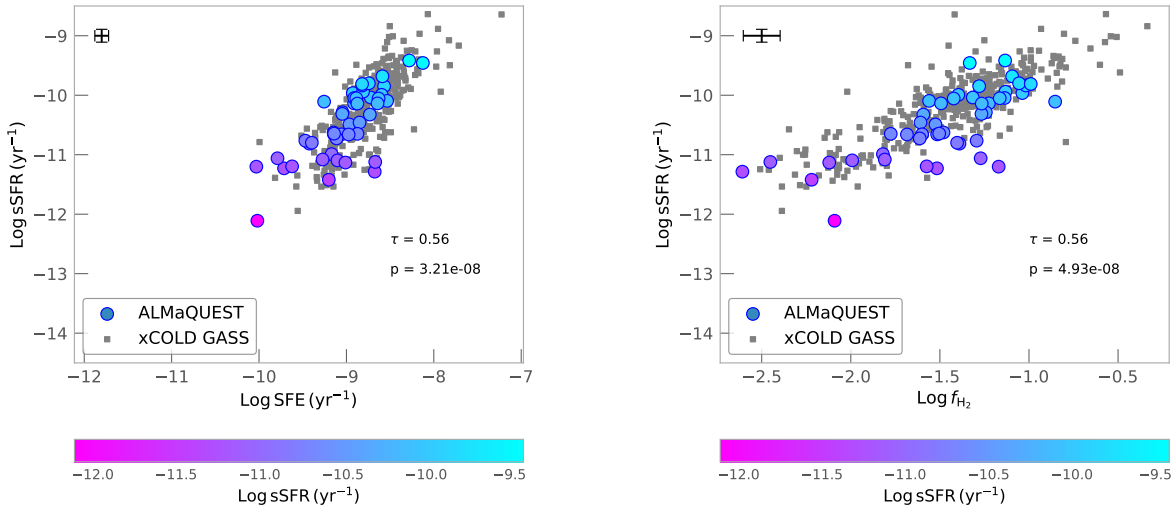

Figure A1. Similar to Figure 4 but with the SFR integrated using all spaxels regardless of the BPT line ratios.

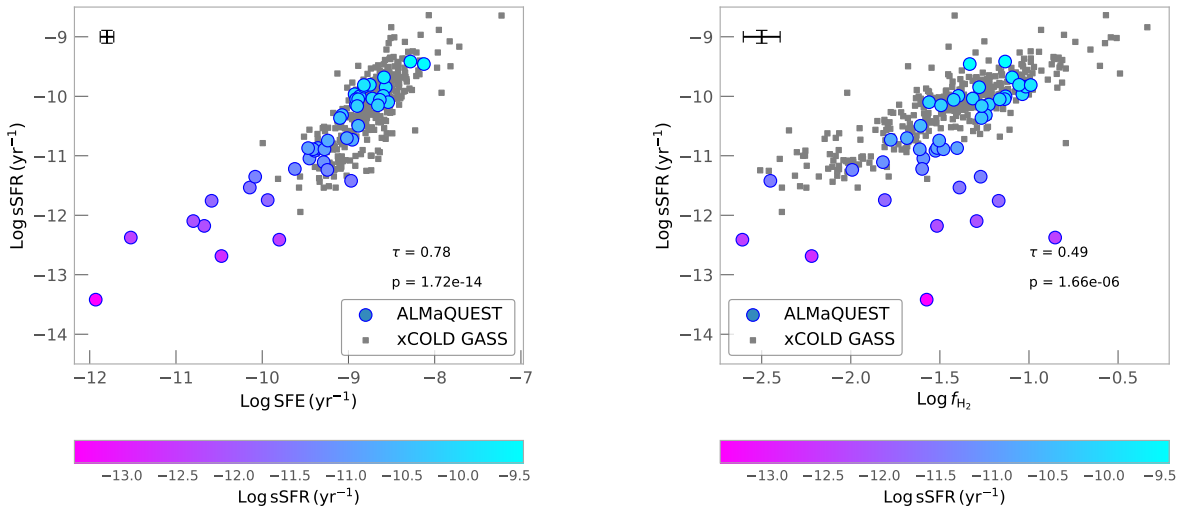

Figure A2. Similar to Figure 4 but with the SFR integrated over star-forming spaxels classified using the [NII] BPT diagnostic (Kauffmann et al. 2003).